A&A 671, A103 (2023)
https://doi.org/10.1051/0004-6361/202244508

Astronomy & Astrophysics

Cosmic metal invaders: Intergalactic O VII as a tracer of the warm-hot intergalactic medium within cosmic filaments in the EAGLE simulation⋆

T. Tuominen[1], J. Nevalainen[1], P. Heinämäki[2], E. Tempel[1,3], N. Wijers[4,5], M. Bonamente[6], M. A. Aragon-Calvo[7], and A. Finoguenov[8]

[1] Tartu Observatory, University of Tartu, 61602 Tõravere, Tartumaa, Estonia
e-mail: tuominen@ut.ee
[2] Tuorla Observatory, Department of Physics and Astronomy, University of Turku, 20014 Turku, Finland
[3] Estonian Academy of Sciences, Kohtu 6, 10130 Tallinn, Estonia
[4] Leiden Observatory, Leiden University, PO Box 9513, 2300 RA Leiden, The Netherlands
[5] CIERA and Department of Physics and Astronomy, Northwestern University, 1800 Sherman Ave, Evanston, IL 60201, USA
[6] The University of Alabama in Huntsville, Huntsville, AL 35899, USA
[7] Instituto de Astronomía, UNAM, Apdo. Postal 106, Ensenada 22800, BC, Mexico
[8] Department of Physics, University of Helsinki, Gustaf Hällströmin katu 2a, Helsinki 00014, Finland

Received 15 July 2022 / Accepted 12 December 2022

ABSTRACT

Context. The current observational status of the hot ($\log T(\mathrm{K}) > 5.5$) intergalactic medium (IGM) remains incomplete. While recent X-ray emission and Sunyaev-Zeldovich effect observations from stacking large numbers of Cosmic Web filaments have yielded statistically significant detections of this phase, direct statistically significant measurements of single objects remain scarce. The lack of such a sample currently prevents a robust analysis of the cosmic baryon content composed of the hot IGM, which would potentially help solve the cosmological missing baryons problem.
Aims. In order to improve the observationally challenging search for the missing baryons, we utilise the theoretical avenue afforded by the EAGLE simulations. Our aim is to get insights into the metal enrichment of the Cosmic Web and the distribution of highly ionised metals in the IGM. Our goal is to aid in the planning of future X-ray observations of the hot intergalactic plasma.
Methods. We detected the filamentary network by applying the Bisous formalism to galaxies in the EAGLE simulation. We characterised the spatial distributions of oxygen and O VII and studied their mass and volume filling fractions in the filaments. Since oxygen is formed in and expelled from galaxies, we also studied the surroundings of haloes. We used this information to construct maps of the O VII column density and determine the feasibility of detecting it via absorption with Athena X-IFU.
Results. Within EAGLE, the oxygen and O VII number densities drop dramatically beyond the virial radii of haloes. In the most favourable scenario, the median extent of O VII above the Athena X-IFU detection limit is ≈700 kpc. Since galaxies are relatively far apart from one another, only ∼1% of the filament volumes are filled with O VII at high enough column densities to be detectable by X-IFU. The highly non-homogeneous distribution of the detectable O VII complicates the usage of the measurements of the intergalactic O VII absorbers for tracing the missing baryons and estimating their contribution to the cosmic baryon budget. Instead, the detectable volumes form narrow and dense envelopes around haloes, while the rest of the O VII is diluted at low densities within the full filament volumes. This localised nature, in turn, results in a low chance (∼10−20% per sight line) of detecting intergalactic O VII with Athena X-IFU within the observational SDSS catalogue of nearby filaments. Fortunately, with deeper filament samples, such as those provided via the future 4MOST 4HS survey, the chances of intercepting an absorbing system are expected to increase up to a comfortable level of ∼50% per sight line.
Conclusions. Based on EAGLE results, targeting the Cosmic Web with Athena may only result in tip-of-the-iceberg detections of the intergalactic O VII, which is located in the galaxy outskirts. This would not be enough to conclusively solve the missing baryon problem. However, the projection of many filaments into a single line of sight will enable a useful X-ray observation strategy with Athena X-IFU for the hot cosmic baryon gas, reducing the amount of baryons still missing by up to ∼25%.

Key words. large-scale structure of Universe – X-rays: general – intergalactic medium – galaxies: halos

1. Introduction

The concordance cosmology model and *Planck* measurements provide very tight constraints for the cosmic baryon density (Planck Collaboration I 2014). When estimating the contributions of different observed baryon components, about half of the expected cosmic baryon budget has until recently remained unaccounted for (Bregman 2007; Shull et al. 2012). This discrepancy has been dubbed the missing baryons problem. In recent years, progress has been made towards the detection of these missing baryons through a wide range of methods. Stacking the *Planck* (Planck Collaboration XXII 2016) thermal Sunyaev-Zeldovich (tSZ) maps between a large number of cluster pairs, de Graaff et al. (2019) and Tanimura et al. (2019) discovered an excess signal attributed to filaments or 'bridges' between the clusters. In a similar vein, Tanimura et al. (2020a)

⋆ Movie associated to Fig. 7 is only available at https://www.aanda.org

detected an excess in the *Planck* tSZ signal by stacking a large number of filaments identified with the DisPerSe filament finding method (Sousbie 2011), inferring the baryon density and temperature of said filaments. Stacking the same filaments with ROSAT (Snowden et al. 1997) background maps, Tanimura et al. (2020b) discovered an X-ray emission signal corresponding to the hot intergalactic medium (IGM). Recently, the dispersion measures of localised fast radio bursts with known redshifts have provided quantitative observational estimates for intergalactic baryon densities (Macquart et al. 2020). These estimates fill the missing baryon gap and thus may provide one solution to the missing baryon problem. In this work we focus on another solution, the direct X-ray absorption detection of the hot phase of the intergalactic diffuse matter, which we define as missing baryons for the purpose of this paper.

Simulations (e.g. Cen & Ostriker 1999; Davé et al. 2001; Dolag et al. 2006; Tepper-García et al. 2012; Martizzi et al. 2019; Galárraga-Espinosa et al. 2021) suggest that the baryon component that had until recently avoided detection consists of the cosmic diffuse baryons in the Cosmic Web. Since the problem is likely due to current observational limits, we divide the diffuse baryonic structure of the Universe into two observationally different domains: (1) the more easily detectable high-density galaxy-scale (∼100 kpc) environment and (2) the observationally more challenging low-density large-scale (∼1−10 Mpc) intergalactic space in the Cosmic Web filaments. Consequently, we propose separating the missing baryon problem into two parts: (1) the galactic missing baryons, related to baryons bound to the galaxies, and (2) the cosmic missing baryons, related to the intergalactic volumes within the Cosmic Web filaments.

Regarding the missing galactic baryons, the Evolution and Assembly of GaLaxies and their Environments (EAGLE) simulations have been used to investigate the detection feasibility of the missing baryons within galaxies via X-ray absorption (Wijers et al. 2020) and emission (Wijers & Schaye 2022). The results indicate that at sight lines passing through a halo of $\log M/M_\odot = 12.0-13.5$ at a radial distance comparable to the halo's virial radius, R_{200}, the column density of the widely used O VII ion is at the level of $\log N_{\rm O\,VII}({\rm cm}^{-2}) \sim 15$. The predicted level is only achievable with the very rare megasecond observations with the currently best instrument for this, the *XMM-Newton*/RGS. Typical 100 ks observations reach only a fraction of this column density level and are thus limited to the central regions. Therefore, a large fraction of the expected baryons in the outer regions of galaxies remain unobserved. According to the EAGLE simulations, future instruments such as the Athena X-ray Integral Field Unit (X-IFU) have the potential to efficiently probe the circumgalactic medium (CGM) within the virial radii of galaxies via O VII absorption and emission (Wijers et al. 2020; Wijers & Schaye 2022). This may enable us to solve to the galactic missing baryons problem.

Cosmological simulations indicate that galaxies (within R_{200}) occupy only ≈1% of the volume covered by the Cosmic Web filaments (e.g. Tuominen et al. 2021). However, due to the orders-of-magnitude higher density of the diffuse baryons in galaxies, compared to that in the filaments (overdensity ∼10), their contribution to the cosmic baryon budget is significant. Namely, ≈25% of the baryon mass contained within the full volumes of the cosmic filaments are concentrated within virial radii of haloes in the EAGLE simulations. Yet, most of the cosmic baryons are located outside R_{200}. Thus, even if the relatively dense galactic environment were one day to be robustly sampled observationally, the cosmic missing baryon problem would still remain unsolved. One cannot use the tips of icebergs to measure the mass of the ice of the sea directly, and similarly one cannot use the measurements of baryons within R_{200} to derive the observational contribution of the intergalactic Cosmic Web volumes outside R_{200} to the cosmic baryon budget[1].

In this work we focus on the cosmic missing baryon problem, in particular on the prospects of detecting the missing baryons in the cosmic filaments via X-ray absorption. According to simulations, a significant fraction of the intergalactic cosmic baryons reside in the hot phase ($\log T({\rm K}) \geq 5.5$) of the warm-hot intergalactic medium (WHIM), corresponding to the X-ray regime. For example, our previous work on EAGLE (Tuominen et al. 2021) yielded that ≈29% of the EAGLE baryon budget is intergalactic hot WHIM, while the SIMBA simulation (Bradley et al. 2022), due to its stronger active galactic nucleus (AGN) jets, gives a bigger fraction of ∼70% for the whole WHIM phase.

The spread of metals into the Cosmic Web relies on the galactic winds driven by supernovae (SNe) and AGN jets. Assuming that the IGM is efficiently enriched by metals, the densities of ions such as O VII and O VIII could be high enough to be detectable with X-rays. These ions could then be used to trace the hot WHIM. In fact, another work based on the EAGLE simulations (Mitchell & Schaye 2022) finds that the mass of the metals ejected from galaxies is substantial; it is comparable to that locked in stars at $z = 0$. The work also finds that most of the ejected metal mass for haloes less massive than $M < 10^{13}\,M_\odot$ is located outside R_{200} at $z = 0$. Tracing the SN-ejected particles in the EAGLE simulations, Kelly et al. (2022) find that ∼35% of the baryons that during cosmic history have been located within the primary halo have, in EAGLE, been ejected outside R_{200} at $z = 0$. For Milky Way-like galaxies, the SN-ejected particles have been expelled to distances of 0.5−1.5 Mpc from the galactic centre. These results suggest the existence of metal-enriched large-scale outflows. We further investigate the ionisation of this component and the distribution of the consequent O VII in the filaments of the Cosmic Web.

Assuming (1) a typical WHIM overdensity of the order of 10 in the filaments and (2) a WHIM temperature $\log T({\rm K}) \sim 6$, it follows that the commonly assumed oxygen abundance of 0.1 solar would yield column densities reaching the level of $\log N_{\rm O\,VII}({\rm cm}^{-2}) = 15$ for typical filament path lengths of the order of 1 Mpc. Since the path lengths through filaments are a factor of 10−100 larger than those through galaxies, the lower densities in filaments may be sufficient to bring the signal above the detection limit of current X-ray instruments in the most optimal situations.

The observational status of intergalactic O VII is poor (see Nevalainen et al. 2019; Nicastro et al. 2022, for recent reviews). Currently, there is no large enough observational sample of intergalactic X-ray ion absorption line measurements of high significance for a meaningful characterisation of the hot WHIM absorber population. This is required to estimate the hot WHIM contribution to the cosmic baryon budget. Because it contains a significant fraction of the cosmic baryons in simulations, and has a poor observational status, the hot WHIM fits the role of the cosmological missing baryons well.

Recent works (Wijers et al. 2019, 2020; Wijers & Schaye 2022) have presented an overview of the metal ion distribution in all environments within the EAGLE simulation, as well as a thorough study of the metal ions within the haloes. In this

[1] One can make assumptions about the distribution of the hot gas in the CGM and in the intergalactic space in the filaments, but an assumption is not a solution to the observational missing baryons problem.

work we take a deeper look into the intergalactic metal ions in EAGLE, in particular within the IGM in cosmic filaments. Martizzi et al. (2019) studied the metal ions in the filaments in the Illustris-TNG simulations, finding 0.1 solar metallicity. We apply a very different approach in the current work. We build on the work of Tuominen et al. (2021), where we characterised the spatial distribution of the hot WHIM and its thermodynamic properties in the cosmic filaments in the EAGLE simulation. In that work we find that the WHIM in the central regions of the densest filaments reaches baryon overdensity levels of ∼10 and temperatures $\log T(\mathrm{K}) \sim 6$, as required for the X-ray detection (see above). In the present work we focus on oxygen, the most common metal in the Universe, and O VII, the most abundant X-ray ion in typical filament environments. By investigating their spatial distributions within the cosmic filaments, we evaluate the column densities in order to derive observational predictions for near-future X-ray instrumentation.

Throughout this work we use $\Omega_\mathrm{m} = 0.31$, $\Omega_\Lambda = 0.69$, $\Omega_\mathrm{b} = 0.048$, $H_0 = 67.8\,\mathrm{km\,s^{-1}\,Mpc^{-1}}$, and $\sigma_8 = 0.83$, given by Planck Collaboration I (2014). These are the same values used in the EAGLE simulations. Since our interest lies in the nearby Universe at redshift $z = 0$, all comoving and proper distances are equal. Thus, we present all distances simply in units of Mpc or kpc.

2. Data

2.1. EAGLE simulation

In this work we used the hydrodynamical EAGLE simulation (Schaye et al. 2015; Crain et al. 2015; McAlpine et al. 2016). In particular, we used the largest simulation run, RefL0100N1504. It followed 1504^3 gas and dark matter particles with initial masses of $m_\mathrm{b} = 1.81 \times 10^6\,M_\odot$ and $m_\mathrm{DM} = 9.7 \times 10^6\,M_\odot$, respectively, within a volume of $100^3\,\mathrm{Mpc}^3$. The N-body simulation code implemented in EAGLE is a modified version of Gadget3 (Springel 2005), with adjustments to the smoothed particle hydrodynamics (SPH) as described in Schaller et al. (2015).

In order to study the baryons within the local Universe, we selected the SPH particles within the snapshot corresponding to redshift $z = 0$. In particular, we studied the smoothed oxygen abundances carried by each SPH particle (see Wiersma et al. 2009a, for a description of the smoothed metallicities). In addition, following Wijers et al. (2019), we combined the simulated oxygen fraction, temperature and baryon density together with tabulated ion fractions to obtain the number of O VII ions within each SPH particle. The ion tables adopted here were created by Bertone et al. (2010) with the use of CLOUDY (Ferland et al. 1998). The tables include the effects of collisional ionisation, as well as photoionisation by a spatially uniform, redshift-dependent ultraviolet (UV) and X-ray background (Haardt & Madau 2001). This is consistent with the radiative cooling model used in EAGLE (Wiersma et al. 2009b).

2.2. Intergalactic oxygen

Since our focus was on the IGM, we needed to draw a border between the galaxies and intergalactic space. The problem is that this procedure is conceptually not well defined. Our practical approach was to utilise the friend-of-friends (FoF) procedure, already applied to the publicly available EAGLE data, which determines whether a given particle is bound to a dark matter halo or not. We considered the non-halo particles as intergalactic in this work.

In more detail, we are interested in the intergalactic metals ejected from galaxies via galactic super-winds and AGN. On the other hand, there are low-metal inflows affecting the metal budget in the outskirts of galaxies. We do not attempt to separate these components. Rather, our pragmatic goal is to characterise the observationally relevant end result of those processes, that is, the total oxygen distribution outside the haloes at $z = 0$. This is sensitive to the implementation of the sub-grid physics, which varies between different simulations. We plan to investigate this issue in a future work by repeating the analyses presented in this work with other simulations with substantially different sub-grid implementations.

Our aim was to study the detection prospects of the intergalactic O VII, done in terms of column densities. We also wanted to probe the three-dimensional information like volume filling fractions provided by EAGLE and this is done in terms of ion number densities. Thus, we needed an order of magnitude estimate for the number density level corresponding to the column density sensitivity limit of current and near-future X-ray instruments. The *XMM-Newton*/RGS is currently the most sensitive X-ray instrument for the O VII absorption measurements. The ∼2% uncertainty in the calibration of the effective area of the RGS (Kaastra 2017) sets the systematic floor for absorption line searches with this instrument. Assuming that a calibration problem causes a spurious 2% dip in the continuum flux within one RGS resolution element (60 mÅ), the feature may be misinterpreted as an astrophysical line with an equivalent width of a few mÅ (Nevalainen et al. 2017). This corresponds to an unresolved Gaussian line with $\log N(\mathrm{cm}^{-2}) \sim 15$. Thus, systematic uncertainties of the RGS effective area calibration do not permit the detection of O VII column densities smaller than $\log N_\mathrm{O\,VII}(\mathrm{cm}^{-2}) = 15$. On the observational side, the exceptionally long (> Ms) exposures of the brightest blazars with RGS have reached the photon statistics corresponding to the above systematic limit set by the instrument calibration (e.g. Nevalainen et al. 2017; Rasmussen et al. 2007). Thus, in this work we adopt $\log N_\mathrm{O\,VII}(\mathrm{cm}^{-2}) = 15$ as the current X-ray detection limit for O VII.

Since most of the intergalactic oxygen (∼76%; see Sect. 3.2) lies within filaments, we estimate the depth through the absorbing material to vary between the order of ∼1 Mpc (a conservative scenario) and ∼10 Mpc (an optimistic scenario) for a filament crossing perpendicular to or along the line of sight, respectively. Thus, we assume that the number density range between $\log n_\mathrm{O\,VII}(\mathrm{cm}^{-3}) = -9$ (for the path of ∼1 Mpc) and $\log n_\mathrm{O\,VII}(\mathrm{cm}^{-3}) = -10$ (for a path of ∼10 Mpc) represents the detectable O VII. In addition, we want to investigate the metal enrichment of the large-scale structure, independently of the ionisation processes. We do this by analysing the oxygen number density distribution above the same numerical range as in the case of O VII. This approach effectively assumes that all oxygen denser than the above cut is ionised to O VII. While this assumption is clearly too optimistic, it provides an approximate way of investigating the large-scale distribution of oxygen related to the observable O VII. We do not utilise this assumption when estimating the actual O VII detection probabilities.

2.3. Column densities

While the number density describes the physical, three-dimensional distribution of the studied ions, what is actually observed in the plane of sky is the two-dimensional projection of these structures. In our case, this corresponds to the integrated ion number densities along the line of sight observed as

O VII column densities. Thus, in order to generate predictions for future observations we produced a set of column densities from the ion number densities in EAGLE.

For this we followed the method described in Wijers et al. (2019). We first divided the simulation box into a set of 20 Mpc long slices along one axis (see Sect. 5 for the motivation for this depth), and subsequently divided each slice into squares of equal width and height along the remaining axes. We settled on a square size of 31.25^2 kpc^2, which is small enough so that results have converged (see Appendix A in Wijers et al. 2019) and large enough to have adequate numbers of particles for robust statistics. The width and height of the squares being much smaller than the depth of the slices, resulted in a number of thin, elongated segments or 'columns'.

The next step was to calculate the O VII densities within each segment. To this end, we had to account for the nature of the SPH particles: each particle represents a volume in space, given by its smoothing length. Thus, we used a smoothing function (i.e. kernel) to distribute the number of ions within each SPH particle to the segment the particle is in and the surrounding segments that are covered by its kernel. Since the end result is a two-dimensional column density map, this smoothing was done only along the plane of the map. Along the direction of the projection we simply positioned all particles in the centre of each segment. Following Wijers et al. (2019), we used a C2-kernel (Wendland 1995), as the same kernel was used for the hydrodynamic properties of the simulated particles in EAGLE. After repeating the process for all the SPH particles and distributing the O VII ions into the corresponding segments, the computed number of ions was divided by the aforementioned area to obtain the column density within each projected segment. Finally, in order to maximise the information from the relatively small EAGLE box, we performed the integration in all 3 orthogonal directions.

2.4. Filaments

In this work we utilised the results of the Bisous filament detection method (Stoica et al. 2007, 2010; Tempel et al. 2014, 2016) applied to the EAGLE galaxy catalogues of McAlpine et al. (2016) as published in Kuutma et al. (2020) and Tuominen et al. (2021). In brief, the Bisous method uses the spatial distribution of galaxies as tracers of the Cosmic Web. It fits cylinders to galaxy overdensities, and subsequently connects and aligns said cylinders. The process is repeated 1000 times to account for the variation due to the stochastic nature of the Bisous method. The regions covered by the cylinders more frequently than an empirically defined critical rate are identified as filaments (Tempel et al. 2014). The Bisous method delivers the volumes and the central spines of the filaments. The current Bisous set-up is fine-tuned for detecting filaments at radial scales of ∼1 Mpc (see Tuominen et al. 2021 for details for testing this with EAGLE).

In order to compare the filaments recreated in EAGLE with the filament catalogue by Tempel et al. (2014), constructed using galaxies in the Sloan Digital Sky Survey (SDSS; Ahn et al. 2014), a magnitude cut (identical to that in Kuutma et al. 2020; Tuominen et al. 2021) was applied. Namely, only galaxies brighter than $M_r < -18.4$ were selected for constructing the Bisous filaments in EAGLE. Essentially, the applied magnitude cut sets a limit for the number density of galaxies (the key property employed by Bisous), and consequently determines the set of detected filaments (Muru & Tempel 2021). By ensuring that the number density of the galaxies used by Bisous was the same for EAGLE and SDSS, we were able to extract a sample of EAGLE filaments comparable to observations.

To test the reliability of the results given by Bisous, Tuominen et al. (2021) studied how Bisous compares to a very different filament finding method, MMF/NEXUS+ (Aragón-Calvo et al. 2007; Cautun et al. 2013). While Bisous uses galaxies as points to trace the filaments, NEXUS+ employs the geometry of a density field (dark matter density for the comparison with Bisous). Despite the very different methods, the thermodynamic properties of the WHIM in the respective filaments agreed within 10%. In a similar vein, Ganeshaiah Veena et al. (2019) compared galaxy properties within Bisous and NEXUS+ filaments using the EAGLE simulation. They found a large overlap in the filamentary galaxy populations, similar fraction of stellar mass within filaments (a difference smaller than 10%) as well as good alignment in the orientation of the filaments detected by the two methods.

However, regardless of the filament finding method, there are great variations in the temperatures and densities between individual filaments detected with the same method (see e.g. Galárraga-Espinosa et al. 2021). Thus, in order to select the most promising filaments to detect the missing baryons, we used the galaxy luminosity density (LD; see Liivamägi et al. 2012) to divide the filaments into low, medium and high LD groups as in Tuominen et al. (2021). As shown in Nevalainen et al. (2015) and Holt et al. (2022), the WHIM density and galaxy LD are tightly correlated. Moreover, the advantage of using the galaxy luminosity to classify filaments comes from its applicability to observations. The LD field was constructed by smoothing each galaxy's luminosity three-dimensionally and evaluating the field at discrete locations, such as the filament spines. The filaments were then divided based on an empirical classification into the aforementioned low, medium and high LD groups. As shown in Tuominen et al. (2021), selecting the filaments within highest LD regions (∼10% of the filaments of the full sample) yields the highest fraction of missing baryons. In the following analysis we used the total filament sample and, when so indicated, the high LD filament group to estimate the benefit of targeting the most WHIM-rich filaments.

3. Oxygen enrichment of the cosmic filaments

We first investigated the distribution of the intergalactic oxygen in the Cosmic Web filaments in the EAGLE simulation. This was done in order to gain an understanding of the metal enrichment of the large-scale structure in the low-redshift universe. We study the ionisation of oxygen separately in Sect. 4. As metals are created in stars within galaxies, from where a fraction of them are ejected towards the IGM, we first characterised their radial extent around haloes. We focused on the oxygen number densities outside the dark matter haloes defined by the FoF algorithm (McAlpine et al. 2016). Subsequently we studied the volume and mass filling fractions of the intergalactic oxygen within the filaments.

3.1. Intergalactic oxygen density profiles around galaxies

Wijers et al. (2020, see their Fig. 2) showed that a significant fraction (≈40%) of the oxygen mass within the whole EAGLE simulation resides outside haloes. In order to quantify in detail the extent of the oxygen distribution in the IGM around haloes, we proceeded to construct radial profiles of the oxygen density

centred at the central galaxy of a given halo[2], defined via the subfind algorithm (Springel et al. 2001; Dolag et al. 2009), and catalogued by McAlpine et al. (2016).

Since we ultimately aim to find the optimal O VII locations for X-ray detection, we selected haloes within the mass range associated with the highest O VII densities. Wijers et al. (2020) showed that the least massive haloes ($\sim \log M_{200}(M_\odot) < 11.5$) have too low virial temperatures compared to the O VII ionisation temperature in order to significantly contribute to the O VII budget. Similarly, haloes with $\log M_{200}(M_\odot) > 13.5$ have too high temperatures and most of the O VII has ionised out. Thus, for the profile we selected haloes within the mass range of $\log M_{200}(M_\odot) = 12-13.5$. In the simulation there is a total of 1282 haloes within this mass range (≈5% of all haloes), with virial radii between 210 and 660 kpc.

We first assigned each non-halo particle to the halo whose centre was closest. We then divided the volume around each mass-selected halo into spherical shells of increasing width and computed the number of non-halo particles in these shells. We used the density profiles around the individual haloes to accumulate a distribution of density values at each given radial shell. We adopted the medians of the distributions in each shell as the representative values for the final oxygen density number profile.

The resulting oxygen density profile decreases rapidly with larger radii (see Fig. 1). At a distance of $r \approx 1$ Mpc, the median oxygen density falls below $\log n_O(\mathrm{cm}^{-3}) \approx -10$. This corresponds to our optimistic observational limit considering an ideal scenario for X-ray observations whereby all of the oxygen in a given filament has been ionised to O VII, and said filament is aligned with the line of sight such that the ion absorption path is 10 Mpc (see Sect. 2.2). In a more realistic scenario of 1 Mpc path through the filament, the median density drops below the detection limit ($\log n_O(\mathrm{cm}^{-3}) \approx -9$) at a distance of $r \approx 500$ kpc, corresponding to $\sim 1-2 \times R_{200}$ in our mass range. The scatter of the densities at a given radius is large due to the wide range of halo masses considered. However, the extent of the detectable oxygen does not exceed 1 Mpc when focusing on narrower mass bins.

3.2. Intergalactic oxygen within filaments

Having characterised the radial intergalactic oxygen density distributions around the central galaxies of the dark matter haloes, our next step was to utilise the knowledge of the distribution of the galaxies in the Cosmic Web in order to understand the metal enrichment in the filaments. Ganeshaiah Veena et al. (2019) showed that in our chosen mass range of $\log M_{200}(M_\odot) = 12-13.5$ (see above), the majority of the haloes in EAGLE are located within the cosmic filaments (see also Cautun et al. 2013, 2014, for a different simulation). Similarly, 76% of the intergalactic oxygen mass in EAGLE is located within Bisous filaments. Thus, if haloes are evenly spaced and are not located too far from one another, it would be reasonable to expect the oxygen to be uniformly distributed within filaments (as regularly done when using X-ray absorption measurements to estimate the baryon content of the filaments).

In order to estimate the average separation between haloes within filaments, we first computed their number density in EAGLE. For haloes within the mass range of $\log M_{200}(M_\odot) = 12-13.5$ and closer than 1 Mpc to any Bisous filament spine, the resulting halo density is $\approx 0.05\,\mathrm{Mpc}^{-3}$. Assuming that they were homogeneously distributed throughout the filaments (i.e. each halo occupying a cube of similar size), the mean distance between haloes would be ≈3 Mpc. In this case, the galaxies would be too widely separated to efficiently enrich the filaments with oxygen.

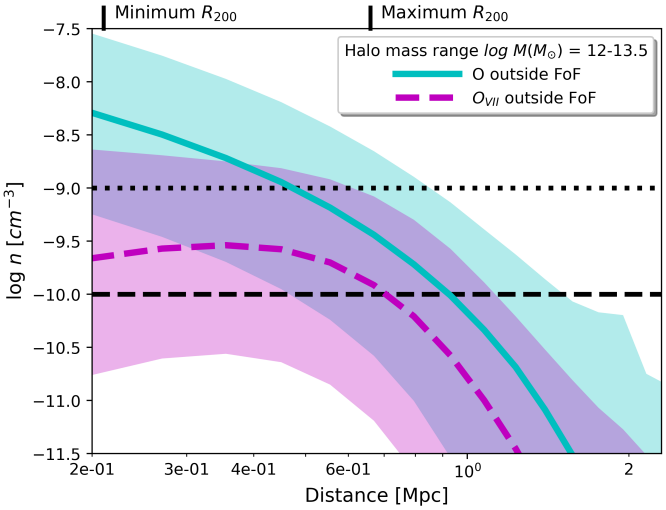

Fig. 1. Median number density (no weighting applied) of the intergalactic oxygen (turquoise line) and O VII (dashed purple line) as a function of distance from nearest halo within Bisous filaments. The shaded regions indicate the 68% scatter in the density distribution from all the filaments combined. Within each distance bin, only particles not belonging to any FoF group were included. Haloes were selected within the mass range $\log M_{200}(M_\odot) = 12-13.5$. The corresponding range of $R_{200} = 220-660$ kpc is indicated on the upper axis. The horizontal dashed lines indicate the approximate detection limits with future X-ray detectors, with the lower and higher limits representing a filament parallel or perpendicular to the line of sight, respectively.

However, in reality the spatial galaxy distribution is far from homogeneous. Namely, along with dark matter and WHIM density, the galaxy density increases from the edge of a filament towards the spine. Thus, to estimate the expected shorter mean galaxy distance at the cores of the filaments due to enhanced mean density, we first computed the number density of central galaxies in the low end of our adopted mass range ($\log M_{200}(M_\odot) = 12.0-12.5$) of EAGLE haloes within a 0.2 Mpc radius of Bisous filament spines. The resulting density was $\approx 0.4\,\mathrm{Mpc}^{-3}$, enhanced by a factor of ∼10 from that within the approximate radius of a filament, $r = 1$ Mpc (see Galárraga-Espinosa et al. 2020; for similar values in a different simulation). This implies a mean distance between low mass haloes of ≈1 Mpc at the core regions of the filaments. This is comparable to the radial extent of the oxygen density above the approximate detection limits. Thus, galaxies may be packed densely enough only at the very core regions of the filaments to efficiently enrich the intergalactic space with oxygen at the detectable levels.

Another obvious deviation of the homogeneous spatial galaxy distribution is due to galaxies clumping into groups. It is a well established observational fact that the larger the galaxy mass and higher its luminosity, the more likely it is found in a group (Tempel et al. 2009). On the other hand, a significant contribution of intergalactic oxygen comes from the high-mass end of our sample. This suggests a clumpy oxygen distribution around galaxy groups. Thus, one would expect spatial segregation: low mass galaxies filling larger filament volumes with oxygen at the core regions of filaments while the high mass galaxies

[2] In most of the cases, the central galaxy coincides with the halo centre.

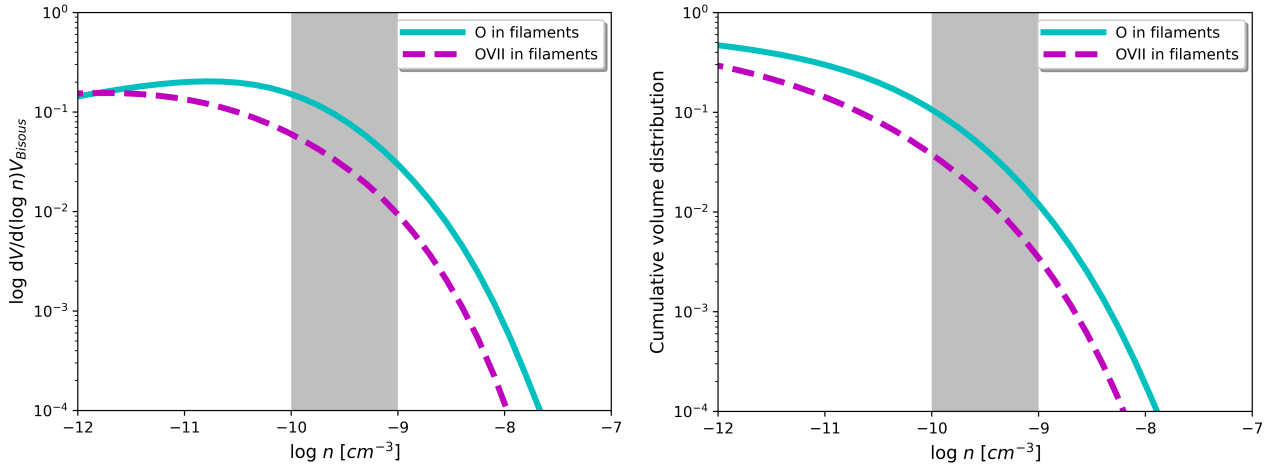

Fig. 2. Filament volume fractions filled by oxygen and O VII. *Left panel*: volume filled by oxygen (turquoise line) and O VII (dashed purple line) at a given number density within the IGM in Bisous filaments, as a fraction of total Bisous volume. *Right panel*: fraction of the volume above a given number density n (cm^{-3}) for oxygen (turquoise line) and O VII (dashed purple line) within Bisous outside haloes normalised by the total Bisous volume. The grey shaded area indicates the assumed observational limits, for a path between 1 Mpc ($\log n \approx -9$) and 10 Mpc ($\log n \approx -10$) along the line of sight.

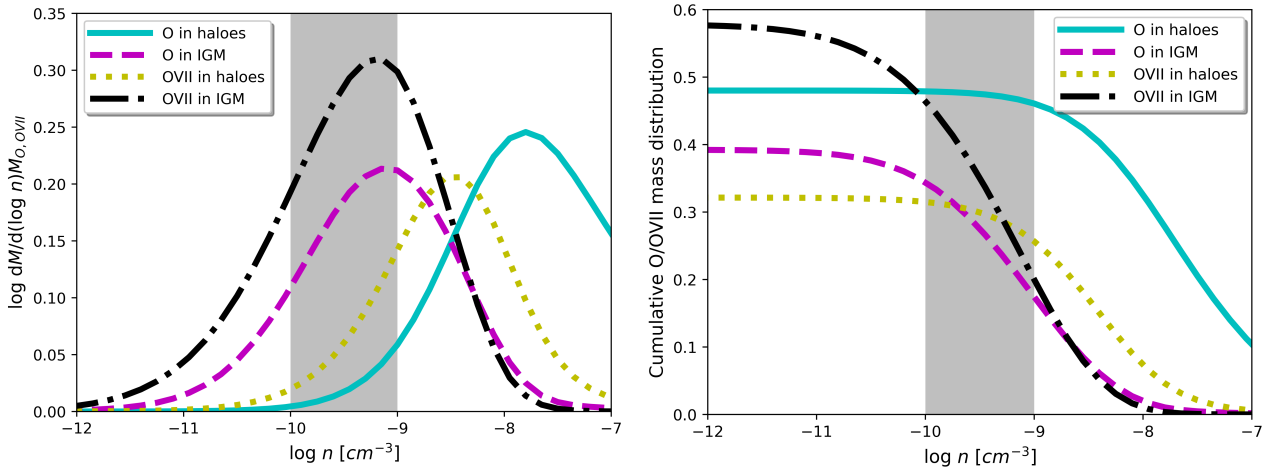

Fig. 3. Oxygen and O VII mass fractions within filaments. *Left panel*: distribution of filamentary oxygen and O VII mass fractions in haloes and the IGM as a function of number density, divided by the total oxygen and O VII mass in the gas phase, respectively. *Right panel*: cumulative mass fraction within Bisous filaments. The sum of oxygen and O VII mass above a given density was divided by the total (non-stellar) mass of oxygen and O VII in the simulation, respectively. In both panels the solid turquoise (dotted yellow) and dashed purple (dash-dotted black) lines refer to the oxygen (O VII) mass within haloes and IGM in filaments, respectively. The grey shaded area indicates the assumed observational limits, for a path between 1 Mpc ($\log n \approx -9$) and 10 Mpc ($\log n \approx -10$) along the line of sight. In both panels we show only the oxygen and O VII distributions within Bisous filaments. The remaining oxygen and O VII are outside the filaments.

add a patchier component (see the next section for the volume filling fractions).

3.2.1. Oxygen volume fractions and mass distributions

We computed the volume filling fraction, that is, how large a fraction of volume within filaments is filled by oxygen above a given density level. To this end, we used the volume covered by individual particles calculated from their SPH variables, by dividing the mass of each simulated particle by its density[3]. Then, the particle volumes above a given density were co-added to obtain a cumulative filament volume filling fraction.

[3] Within Bisous filaments, the sum of the volumes of individual particles equals the total volume covered by the filaments (≈5% of the total simulation volume).

We found that when considering the total Bisous filament volumes, (i.e. also including volumes within haloes), ≈11% is filled with oxygen (see Fig. 2) at densities above $\log n_{\rm O}({\rm cm}^{-3}) = -10$ (i.e. at approximately the currently detectable level in optimal conditions; see Sect. 2.2), while only 1% above the more realistic limit $\log n_{\rm O}({\rm cm}^{-3}) = -9$. Thus, the worrying indication seen in EAGLE is that most of the Cosmic Web filament volume appears to contain oxygen below the current detection threshold, with oxygen above the limit forming relatively narrow envelopes around the haloes.

We proceeded to better understand the implied low filament volume filling fraction of detectable oxygen. To this end, we computed the oxygen mass distribution as a function of density within filaments, separately for haloes and the IGM. In filamentary haloes (i.e. haloes within the Bisous filaments), the oxygen distribution peaks at a density of $\log n_{\rm O}({\rm cm}^{-3}) \approx -7.8$ (Fig. 3,

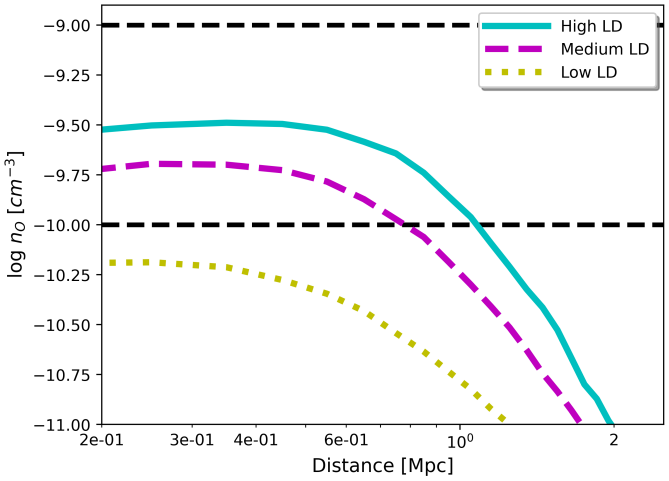

Fig. 4. Number density (n_O) profiles of the intergalactic oxygen as a function of distance from filament spines. Each profile represents the median value from the individual spines at each given distance bin, with turquoise, dashed purple, and dotted yellow lines showing the median values for high, medium, and low LD filaments, respectively. The approximate detection limit range is shown with horizontal dashed lines.

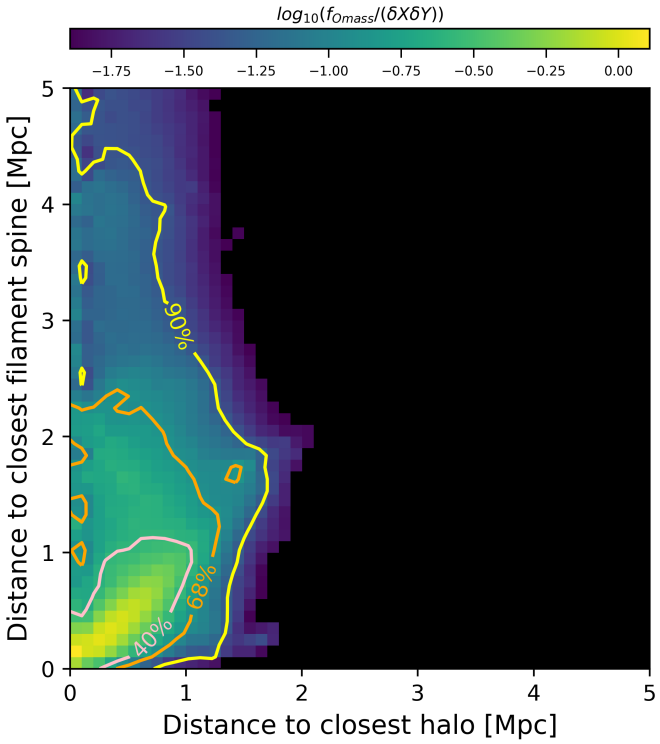

Fig. 5. Oxygen mass fraction towards halo centres and filament spines. Each simulated particle was positioned within one pixel in the diagram based on the distance to its closest halo centre and filament spine. Subsequently, the oxygen mass contained in the particles was co-added within each pixel and divided by the pixel size. Finally, the value in each pixel was normalised with the highest value in the diagram. The colour map shows values down to 1% of the peak value. The pink, orange, and yellow contour lines enclose 40%, 68%, and 90% of the oxygen mass, respectively.

left panel). On the other hand, the intergalactic oxygen peaks at an order of magnitude lower density of $\log n_O(\mathrm{cm}^{-3}) \approx -9.1$. Integrating the distributions we found that a significant fraction (between 20 and 35%) of the total oxygen mass in the EAGLE simulations lies within the filamentary IGM above the approximate current X-ray detection limit (Fig. 3, right panel). This corresponds to ≈50−85% of the total intergalactic oxygen mass, which we found in Sect. 3.2.1 to cover only 1−11% of the filament volumes. Thus, the intergalactic oxygen peak probably corresponds to small and dense pockets around haloes (see Sect. 4.2 for the radial distribution of O VII).

3.2.2. Oxygen density profiles around filament spines

Since (1) the galaxy density increases when approaching the spine of the filament (e.g. Galárraga-Espinosa et al. 2020) and (2) the oxygen density at detectable levels is confined within 1 Mpc of the halo centre, it is expected that the oxygen density increases towards the filament spines. In order to quantify the expected radial dependence of the oxygen density we proceeded to create radial oxygen density profiles as a function of distance from the filament spines. As our region of interest lies in the IGM, we selected only simulated particles outside FoF haloes. Analogously to the halo profiles in Sect. 3.1, each particle was assigned to its closest filament spine from which the distance was calculated. The subsequent profiles were done in a similar fashion to Tuominen et al. (2021) for the baryon density, that is, separating the volumes around filament spines into concentric hollow cylinders, and dividing the total number of oxygen atoms within each cylinder by its volume. In addition, we removed the volumes covered by the removed haloes from each concentric cylinder. After computing the radial profiles for individual filament spines, we selected the median density value at each distance bin, thus producing a single profile. This was done separately for filaments in different LD groups (see Sect. 2.4 for the different LDs).

Similarly to the halo profiles, the oxygen density profiles in filaments peak at the spine and decrease rapidly with radius (Fig. 4). Moreover, high LD profiles yield oxygen densities ≈2 and ≈5 times greater than medium and low LD profiles, respectively. This is to be expected, as filaments within higher LD regions contain more galaxies and therefore more stars producing oxygen, which is then expelled into the IGM. The oxygen density for medium and high LD regions remains above the limit of $\log n_O(\mathrm{cm}^{-3}) = -10$ up to a distance of $r = 1$−1.2 Mpc from the spine. However, the profiles do not reach the more realistic limit of $\log n_O(\mathrm{cm}^{-3}) = -9$. This suggests that not even the high luminosity filaments, containing most of the hot WHIM (Tuominen et al. 2021), enclose enough oxygen to be detected perpendicular to the line of sight.

We then proceeded to connect the oxygen density profiles around filament spines to those around haloes. To this end, we computed a mass diagram that reveals the oxygen distribution with respect to the distance to both halo centres and filament spines (Fig. 5). Within ≈1 Mpc from filament spines and haloes there is a correlation in the oxygen mass. This can be explained by the fact that haloes (from where oxygen is expelled) tend to reside along or nearby the filament spines. However, this correlation between spines and haloes disappears at larger distances. For haloes, only ≈4% of the total oxygen mass lies beyond 1.5 Mpc, while oxygen can be found at larger distances from filaments. Indeed, ≈38% of the oxygen mass can be found further than 1.5 Mpc from the filament spines. At the same time, within our chosen mass range of $\log M_{200}(M_\odot) = 12$−$13.5$, ≈40% of haloes reside further than 1.5 Mpc from any filament spine. This indicates that oxygen is more tightly related to the haloes where

it is formed, and filaments play only a secondary role in its distribution. This also raises the question of the environment where these non-filamentary haloes and oxygen reside. While potentially most are in the nodes of the Cosmic Web (not traced by the Bisous method), a significant fraction might be in low-density regions and voids. However, this is beyond the scope of this work, since our aim is to trace the hot IGM, contained mainly within filaments. Thus, we moved on to examine the ionisation of oxygen into O VII, the dominant ion at the hot WHIM temperatures.

4. Ionisation of the cosmic oxygen

Given the above characterisation of the intergalactic oxygen, we proceeded to studying the ionisation of the cosmic oxygen via O VII distributions and temperature analysis.

4.1. Thermodynamic large-scale structure

Theoretically, the heating mechanisms of the intergalactic baryon gas in filaments are well established. The most important process in this context is the shock-heating arising from the accretion of the baryons towards the filaments pulled by the dark matter gravity (e.g. Ryu et al. 2003). The baryons falling towards the filaments also experience adiabatic compressional heating. Both effects are stronger closer to the maxima of the gravitational potential, that is, the filament spines. This region is thus expected to harbour the hottest WHIM, as consistently demonstrated by numerous cosmological simulations (e.g. Cen & Ostriker 1999; Davé et al. 2001; Dolag et al. 2006; Branchini et al. 2009; Cui et al. 2012, 2018; Tuominen et al. 2021; Haider et al. 2016). The SN and AGN feedback as well as halo mergers provide additional heating in the close neighbourhood of galaxies.

To give a quantitative example, Tuominen et al. (2021) showed that the density and the temperature of the intergalactic gas in the EAGLE simulations peak at the filament spines. When focusing on the inner ∼1 Mpc regions around the densest filament sample, the temperatures reach a level of $\log T(\mathrm{K}) \approx 5.5{-}6.0$ (i.e. the energies of most of the free electrons exceed the ionisation energy of O VII). The baryon overdensities in these regions reach the level of ∼10. In these conditions O VII is mainly produced via collisional ionisation (e.g. Strawn et al. 2023). The demonstration that the oxygen density also peaks in these regions (see Sect. 3.2.2) suggests that the optimal place to look for the missing baryons in the form of the hot WHIM in X-rays are the central regions of the densest filaments.

We performed here a quantitative temperature analysis in order to understand better the above described scenario of the ionisation of the cosmic oxygen. Indeed, we found that the majority (≈72%) of the oxygen mass considering the full intergalactic volumes within filaments has a temperature above $\log T(\mathrm{K}) > 5.5$ (see Fig. 6), required for O VII production under collisional ionisation equilibrium (CIE). Assuming CIE, almost all of the oxygen is expected to be ionised to O VII within the temperature range of $\log T(\mathrm{K}) = 5.5{-}6.2$, while O VIII begins gaining ground at higher temperatures (Mazzotta et al. 1998). We found that ≈50% of the intergalactic EAGLE oxygen mass is in this temperature range. However, the intergalactic O VII mass fraction is smaller (≈33%), implying that the ionisation responsible for the O VII population is not purely CIE from a single phase gas.

The very low density of the filamentary IGM (density contrast $\delta \sim 1{-}100$) is probably responsible for the relatively low efficiency of the O VII production. The efficiency of the collisional ionisation decreases relatively fast with lower densities, as it is proportional to the density squared. Consequently, the collisional ionisation timescale is comparable to the Hubble time at a density contrast $\delta \sim 10$ and exceeds it significantly at lower densities (e.g. Bykov et al. 2008). On the other hand, photoionisation begins to play a more significant role at lower densities due to its linear dependence on the ion density. Towards lower densities, the UV background photon density per particle increases and thus a larger fraction of O VII is produced via photoionisation (e.g. Nelson et al. 2018; Wijers et al. 2019; Strawn et al. 2023). However, only the high-energy tail of the UV background photons exceeds the ionisation energy of O VII (Haardt & Madau 2001), and therefore this effect does not compensate for the inefficiency of CIE in the production of O VII. Additional factors, such as further photoionisation by the X-ray background, may also play a role, but they are beyond the scope of this work.

Conversely, the bulk of the oxygen in the FoF haloes is hotter: most of the oxygen mass is at $\log T(\mathrm{K}) > 6$ (see the upper-right panel in Fig. 6). Due to the very high temperatures, most of the oxygen is expected to be further ionised beyond O VII. Indeed, the fraction of oxygen in the form of O VII in haloes is ≈12%, much smaller than in the intergalactic space.

4.2. Intergalactic O VII around galaxies

While the core regions of filaments have ideal temperatures for O VII, according to EAGLE the oxygen density distribution above the level approximately achievable with current and near-future X-ray detectors is highly inhomogeneous (see Sect. 3.1). It peaks at the locations of the haloes and drops rapidly below the detection level as a function of distance from the halo.

In order to quantify the radial behaviour of O VII around haloes, we constructed an O VII density profile following the method we applied to oxygen (i.e. choosing only particles that reside in the IGM around haloes within a mass range of $\log M_{200}(M_\odot) = 12{-}13.5$). We found that beyond the virial radius R_{200}, the O VII density drops rapidly below the optimistic observational limit of $\log n_{\mathrm{O\,VII}} < -10$ at a radial distance of ≈700 kpc (see Fig. 1). Considering the conservative observational limit of $\log n_{\mathrm{O\,VII}} < -9$ the picture is even bleaker, as the median density profile does not reach that level at any radii. The visual investigation of the three-dimensional distribution of O VII density indeed confirms the relatively low radial extent of O VII at detectable levels (see Fig. 7).

The analysis above indicates that the envelopes containing detectable amounts of O VII are very tightly constrained around the haloes. A similar conclusion can be derived from a work on the high-resolution HESTIA simulation (Damle et al. 2022). It is a simulation of the Local Group, with the Milky Way and Andromeda galaxies, that indicates that the median O VII column density profile drops below the $\log N_{\mathrm{O\,VII}}(\mathrm{cm}^{-2}) = 15$ level beyond $\sim 3 \times R_{200}$ from the halo centre (their Fig. 4 Damle et al. 2022). In fact, the EAGLE O VII envelopes are narrower than those of oxygen (Fig. 1). Indeed, not all oxygen is ionised into O VII, but instead there is a spatial co-existence of different temperature phases as well as limiting effects on the ionisation efficiency.

4.3. Intergalactic O VII within filaments

Given that the ionisation acts as an additional constraint and thus the median O VII density profile around haloes remains lower than the oxygen density at all radii, we repeated the analysis of

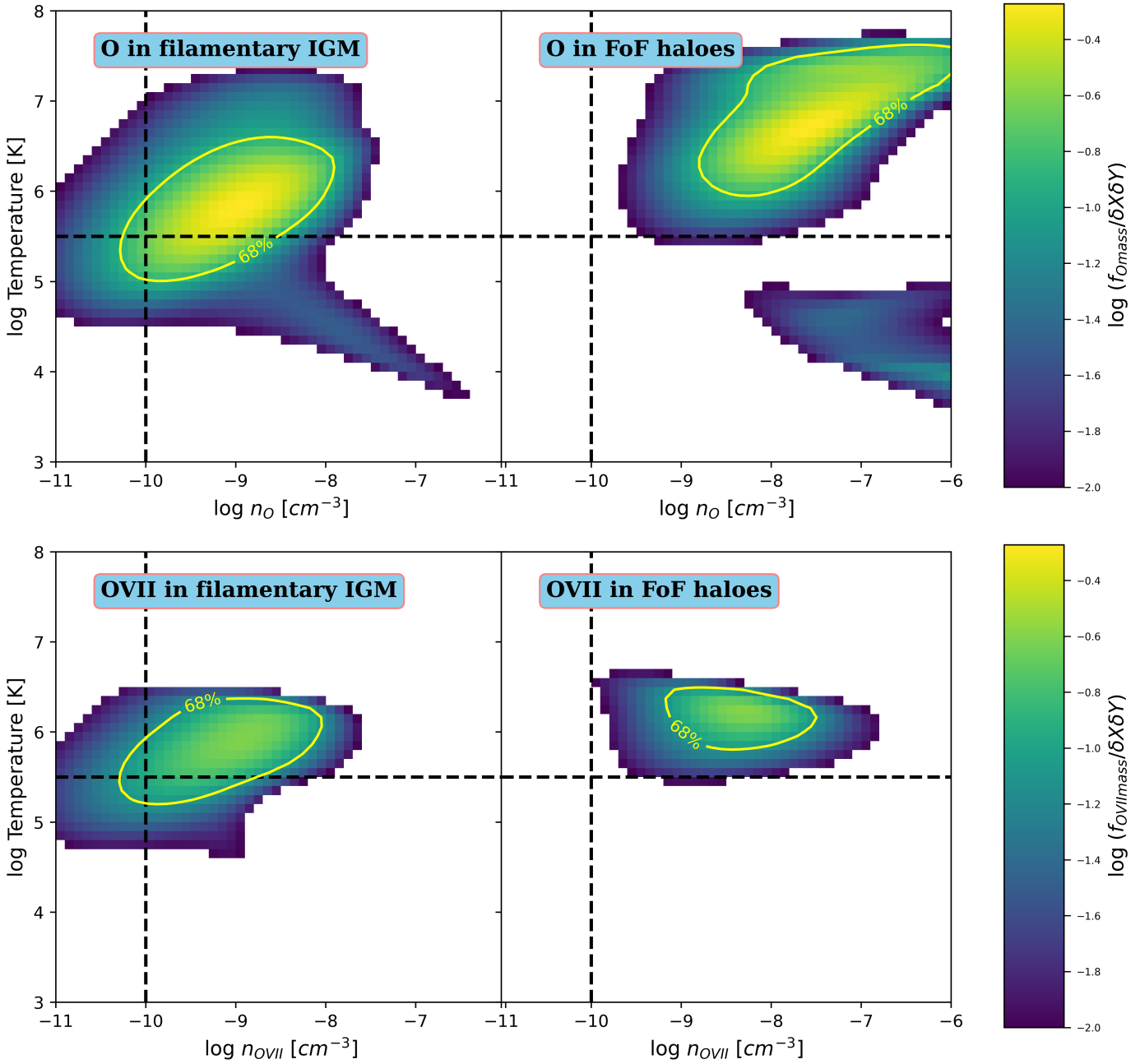

Fig. 6. Distribution of oxygen (*upper panel*) and O VII (*lower panel*) mass as a function of number density and temperature. The *left panels* show the oxygen and O VII distributions in the IGM within Bisous filaments. Gas in FoF haloes is shown in the *right panels*, where we selected haloes located within Bisous filaments. The colour scales indicate the fractions of oxygen and O VII mass over the total oxygen mass in the same environment (divided by pixel area; values are shown down to 1%). The yellow circles mark the regions where 68% of the given mass is contained. The horizontal and vertical dashed lines mark the limit for the hot gas (log T(K) > 5.5) and the optimistic lower density limit for X-ray observations (given a 10 Mpc long path aligned with the line of sight), respectively.

mass distributions and volume filling fractions for O VII within filaments (see Sect. 3.2.1 for the oxygen volume and mass fractions). Additionally, we computed the fraction of hot WHIM that could potentially be traced with O VII.

4.3.1. O VII volume fractions and mass distributions in filaments

In a similar fashion to oxygen, the intergalactic O VII mass distribution peaks at $\log n_{\mathrm{O\,VII}}(\mathrm{cm}^{-3}) \sim -9$ (see the left panel in Fig. 3), at the upper boundary of the estimated detection limit (see Sect. 2.2). Above this density limit, approximately 20% of all the O VII mass in the whole simulation is contained within filaments (see Table 1 and right panel in Fig. 3). Moreover, ≈45% of the O VII is within filaments above a density limit of $\log n_{\mathrm{O\,VII}} > -10$. This corresponds to ≈77% of the total intergalactic O VII (i.e. outside haloes; see Fig. 6). However, considering that the median density drops rapidly as a function of distance from haloes, this O VII mass is contained within small pockets.

Indeed, only 4% and 0.4% of the full EAGLE filament volume is filled by O VII with densities above $\log n_{\mathrm{O\,VII}} = -10$ and

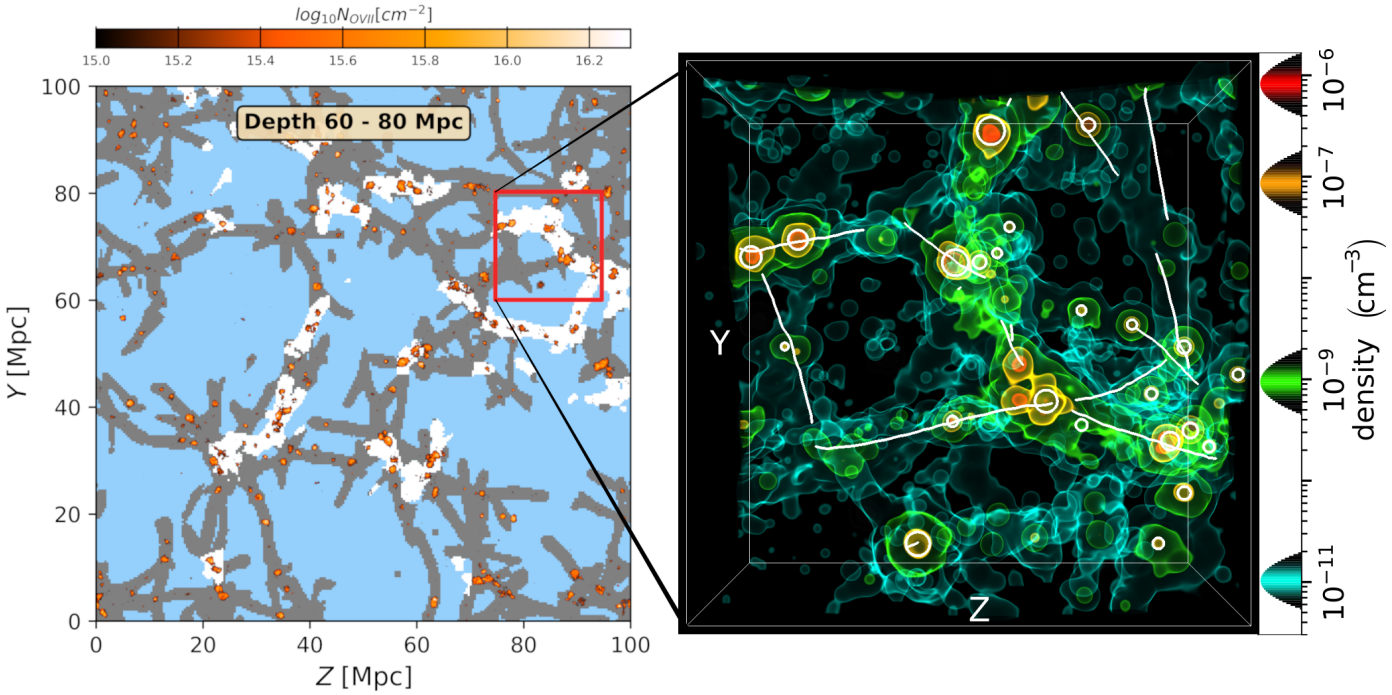

Fig. 7. Comparison between the two-dimensional column densities and the three-dimensional number densities of O VII. *Left*: column densities of O VII projected through a 20 Mpc deep slice along the *x*-axis. The colour scheme indicates the O VII column density with a lower limit at $\log N_{\rm O\,VII}(\rm cm^{-2}) = 15$, while the Bisous filaments and high LD Bisous filaments are shown by grey and white areas, respectively. This image is the same as the middle-right panel of the column density maps in Fig. 9. The red square corresponds to the volume shown in the right-hand figure. *Right*: three-dimensional visualisation of the O VII distribution in a $(20\,\rm Mpc)^3$ zoom-in box within the larger EAGLE volume. The coloured regions represent the O VII density contours at given values, as indicated on the right vertical axis. The green contour shows the spatial extent of O VII above the optimistic detection limit of $n_{\rm O\,VII} = 10^{-9}\,\rm cm^{-3}$ discussed in the text. The white lines show the Bisous filament spines, while the white circles indicate the volumes within R_{200} around the central galaxies of the FoF haloes. A three-dimensional visualisation is available as an online movie.

−9, respectively (see Fig. 2, right panel). At the higher density limit, a path of the order of 1 Mpc is enough to result in detectable column densities, thus rendering the halo outskirts observable. Consequently, the filamentary O VII density above the expected detection levels is very patchy, which is evident in the column density maps (see the right panel in Fig. 8 and all panels in Fig. 9; see Sect. 2.3 for the details of producing the maps). Furthermore, the three-dimensional distribution reveals how the filament volumes are largely devoid of O VII above detectable levels (see Fig. 7).

Thus, assuming that EAGLE captures accurately the distribution of O VII in the Cosmic Web filaments, the above results have important consequences for the missing baryon detection. Namely, the essential assumption when evaluating the cosmic baryon content based on X-ray absorption measurements is that O VII is well mixed into the WHIM. This assumption is not valid above the current and expected near future detection limit of $\log N_{\rm O\,VII}(\rm cm^{-2}) > 15$. Consequently, the projected sky area of the volumes filled by O VII is relatively small at the detectable level, rendering its observation challenging (see Sect. 5 for the feasibility study).

4.3.2. Hot WHIM traced by O VII

Ultimately, our aim was to quantify the amount of the hot WHIM traceable with O VII absorption. Indeed, most of the intergalactic O VII mass is contained above the temperature limit for the hot WHIM ($\log T(\rm K) > 5.5$) and above the approximate detection limit of $\log n_{\rm O\,VII}(\rm cm^3) > -10$ (lower panel in Fig. 6). However, since the O VII density decreases rapidly as a function of distance from the nearest halo (see Fig. 1), the volume covered by O VII remains low. On the other hand, the hot WHIM density is also expected to peak around haloes. To further investigate this, we generated a hot WHIM density profile around haloes within a mass range of $\log M_{200}(M_\odot) = 12{-}13.5$ in the same way as for O VII (see Sect. 3.1 for a description of the procedure). For a better comparison between hot WHIM and O VII, we normalised the densities with their median value at R_{200}, $\log \rho_{\rm WHIM}(M_\odot/\rm Mpc^3) \approx 12$ for the hot WHIM and $\log n_{\rm O\,VII}(\rm cm^3) \approx -9.3$ for O VII. This yielded that both the hot WHIM and O VII densities decrease fast with distance from the halo with a similar trend until $\approx 2 \times R_{200}$, and slightly deviate beyond that (see Fig. 10). This would imply that a large fraction of the O VII and hot WHIM masses are located close to said haloes. Consequently, this suggests that we may be able to trace some of the missing baryons via O VII in the surroundings of haloes.

To uncover whether O VII and the hot WHIM are indeed spatially connected, we computed the mass fraction of the hot WHIM in Bisous filaments that is contained within the same volumes as O VII above $\log n_{\rm O\,VII}(\rm cm^3) > -10$. From all the hot WHIM, ≈27% is spatially collocated within the same volumes as O VII above the aforementioned density limit. Thus, O VII may be used to trace up to a quarter of the missing baryons. This, in turn, corresponds to ≈6% of all the baryons in the EAGLE simulation. While the next generation of X-ray instruments will not be able to trace all of the missing baryons within the hot WHIM with O VII absorption, they will push the limits of the

Table 1. Volume filling fractions and mass fractions of the intergalactic oxygen and O VII within Bisous filaments above the detectable densities.

	$\log n(\mathrm{cm}^{-3}) > -9$	$\log n(\mathrm{cm}^{-3}) > -10$
O volume	1%	11%
O mass	20%	35%
O VII volume	0.4%	4%
O VII mass	20%	45%

Notes. All masses are given as fractions of the total mass within the simulation.

observable beyond the virial radius and halo outskirts to the truly intergalactic regime. At the more realistic limit of $\log n_{\mathrm{O\,VII}}$ $(\mathrm{cm}^3) > -9$, however, the filamentary volume covered by the intergalactic O VII is ten times smaller. As a consequence, the fraction of hot WHIM traced by O VII is much smaller, ≈7%, which corresponds to ≈1% of the total baryon budget. Therefore, for the hot WHIM to be properly traced by O VII, filamentary haloes ought to be close enough to one another and the filament itself to be aligned with the line of sight.

5. Column densities of the intergalactic O VII and the detection prospects with Athena

We utilised the above three-dimensional characterisation of the distribution of O VII to obtain insights for the observational search of the intergalactic missing baryons via X-ray absorption. Even though the above EAGLE-based indication is that targeting filaments may only result in the tip-of-iceberg detections of O VII in the galaxy outskirts, the projection of large volumes into the sight line may still make a useful X-ray observation strategy for the hot cosmic baryon gas possible.

We focus on the absorption feasibility with the X-IFU instrument on board European Space Agency's planned future X-ray mission Athena. Since our estimates are broad and based only on the order-of-magnitude detection limit of O VII, the Athena estimates are approximately valid for the planned future missions ARCUS[4], HUBS[5], and Lynx[6], which are also expected to have similar capabilities. Specifically, Lynx and HUBS will feature microcalorimeter arrays with spectral resolution in the soft X-ray band that is similar to that of Athena's X-IFU (∼1–2 eV resolution Gaskin et al. 2019; Cui et al. 2020). Lynx will also feature a grating spectrometer with sub–eV resolution, similar to the one that is proposed for the Arcus mission (Smith et al. 2019), both with significantly higher resolution and collecting area than the current–generation grating spectrometers on board *XMM-Newton* and *Chandra*. Thus, Arcus and Lynx may be able to extend the O VII absorption work to lower column densities. We thus report the basic results also for lower detection limits in Table 2.

The required 2.5 eV spectral resolution of X-IFU (Nandra et al. 2013; Barret et al. 2018) corresponds to a redshift resolution of $\Delta z = 0.005$ at 0.5 keV, which in turn corresponds to a spatial resolution of ≈20 Mpc at low redshifts. Following the procedure described in Sect. 2.3, we sampled the O VII column densities into $20\,\mathrm{Mpc} \times 31.25^2\,\mathrm{kpc}^2$ segments, which we interpret as individual X-IFU absorbers. The result

[4] http://www.arcusxray.org/
[5] http://hubs.phys.tsinghua.edu.cn/en/index.html
[6] http://www.lynxobservatory.com/

Table 2. Probability, $P_{N(\mathrm{O\,VII})}$, of intercepting at least one absorber above a given column density limit per sight line for a depth of 120 and 600 Mpc, which corresponds to the SDSS and 4MOST 4HS surveys, respectively.

Min. $\log N_{\mathrm{O\,VII}}$	120 Mpc	600 Mpc
14.0	50% (72%)	98% (98%)
14.5	28% (48%)	80% (85%)
15.0	11% (22%)	45% (50%)
15.5	1.5% (4%)	8% (10%)

Notes. The probability of intercepting one absorber targeting high LD filaments is indicated in brackets.

is a set of two-dimensional O VII column density maps (see Figs. 8 and 9). This process was repeated along the remaining orthogonal directions (projecting along the Y- and Z-axes) to create a total of 15 column density maps.

As mentioned in Sect. 4.3.1, the column density maps of individual absorbers are very patchy above the limit of $\log N_{\mathrm{O\,VII}}(\mathrm{cm}^{-2}) = 15.0$ (panels 1–5 in Fig. 9). Indeed, most of the filaments (in grey and white for all and high LD filaments, respectively) are devoid of O VII above the detection limit. When considering a projection through the whole simulation box (100 Mpc, right panel in Fig. 8 and last panel of Fig. 9), the picture is somewhat better, as structures from different slices are combined. But it is still far from optimal, as most of the filaments remain empty.

In order to quantify the distribution of the intergalactic O VII absorbers (see above for the definition of an absorption system used here), we computed its column density distribution function (CDDF). The CDDF is defined as follows:

$$f(N, z) \equiv \frac{\partial^2 n}{\partial \log N \partial z}, \tag{1}$$

where n corresponds to the number of absorbers, N is the column density (in our case of O VII) and z is the redshift. To investigate the environmental distribution of the O VII absorbers in the Cosmic Web, we calculated the CDDFs for (1) all the O VII absorbers, (2) intergalactic O VII within Bisous filaments, and (3) O VII within FoF haloes in Bisous filaments.

We found that at the low values the distributions decrease relatively slowly with increasing column density but beyond a break at $\log N_{\mathrm{O\,VII}}(\mathrm{cm}^{-2}) \approx 15.8$ they decrease steeply (see Fig. 11). The O VII column densities below the break are dominated by the intergalactic gas while above the break the dominating source is the gas within haloes. Indeed, Wijers et al. (2020) describe the break (or 'knee') as a transition from gas within haloes to the IGM. While they concentrated on the halo component, our focus here is the IGM within filaments.

In order to derive properly the cosmologically interesting information about the number of absorption systems per unit redshift dz one should analyse a deep enough light cone simulation so that (1) the sampled volume is substantial in order to minimise the cosmic variance and (2) the possible redshift evolution of the absorbers would be included. The $(100\,\mathrm{Mpc})^3$ snapshot at $z = 0$ studied in this work has very limited use for this purpose. However, for comparison with other works, keeping the above caveats in mind, we performed the exercise of integrating the CDDF (Eq. (1) and Fig. 11). We found that when considering all intergalactic O VII, there are ≈4 absorbers per unit redshift at $\log N_{\mathrm{O\,VII}}(\mathrm{cm}^{-2}) > 15$. The comparison of this value to other works is complicated due to, for example, varying definitions of

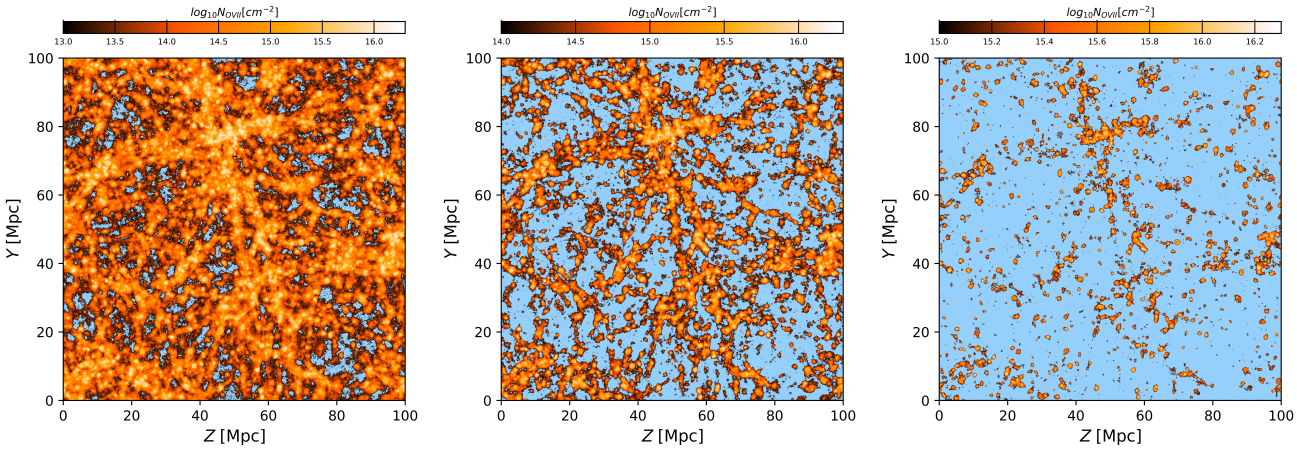

Fig. 8. Projection of the O VII column densities across the EAGLE volume (100 Mpc), with a lower limit of $\log N(\mathrm{O\,VII}) > 13$ (*left panel*), $\log N(\mathrm{O\,VII}) > 14$ (*middle panel*), and $\log N(\mathrm{O\,VII}) > 15$ (*right panel*).

an absorber and treatments of the haloes and intergalactic matter. Yet, our estimate is similar to those obtained by Branchini et al. (2009), Cen & Ostriker (2006), and Wijers et al. (2019).

As discussed in Sect. 4.3.1, most of the intergalactic O VII lies within filaments. What is more, around the observable level of $\log N_{\mathrm{O\,VII}}(\mathrm{cm}^{-2}) > 15$ the intergalactic component of the CDDF is completely dominated by gas within Bisous filaments. This means that virtually all observable intergalactic O VII is located within filaments.

In the following sections we provide observational predictions for these filamentary O VII column densities in two different large-scale surveys, SDSS and 4-m Multi-Object Spectroscopic Telescope (4MOST) survey.

5.1. SDSS

Given that the observational X-ray absorption signals are presumably very weak, it is important to detect the filaments harbouring the hot WHIM in optical surveys. This provides the redshift for the absorber, which helps identify the spectral line and to constrain the physical properties of the absorber. In addition, the knowledge of the large-scale environment aids in confirming the intergalactic nature of the absorber.

We consider first the Bisous filament catalogue of Tempel et al. (2014), constructed from SDSS galaxies, which is quite complete up to redshift $z = 0.05$, corresponding to a depth of ≈215 Mpc. The filament catalogue starts from a radial distance of ≈85 Mpc in order to avoid the Local Void, an underdense region surrounding our Milky Way. Thus, the radial depth of the filament sample is ≈130 Mpc, slightly larger than the EAGLE simulation box.

In order to quantify the feasibility of the observational search for the missing baryons we first calculated the fraction of the SDSS footprint covered by filaments. To this end, we randomly selected 10 000 sight lines through the plane of sky covered by SDSS and found that a vast majority (≈92%) of such sight lines cross a filament at least once (see Fig. 12, bottom-left panel). When considering only the high LD filaments (i.e. filaments harbouring a larger fraction of missing baryons; see Sect. 2.4), this covering area is ≈23% of the whole survey (Fig. 12, bottom-right panel).

In order to estimate how accurately the observational SDSS filament network geometry (i.e. number densities and extents of the filaments) are reproduced by the EAGLE simulations, we repeated the area covering analysis for filaments in the simulation. We applied the same Bisous method for detecting both the observational and the simulated filaments. To this end, we again selected 10 000 random sight lines crossing the simulation through a random orthogonal direction (X, Y or Z), and adjusted for the difference in the SDSS and EAGLE depths. Of all the sight lines, ≈91% and ≈23% cross at least once a filament or a high LD filament, respectively (Fig. 12, top panels). Thus, the projected areas covered by filaments in SDSS and EAGLE are consistent within ∼1%. The excellent agreement gives us confidence that the basic geometric properties of filaments (the number density and the extent) are accurately reproduced in the EAGLE simulations. This justifies the usage of EAGLE filaments as a basis for making predictions for the baryon content of the Cosmic Web filaments.

We then proceeded to examine the column densities along the random sight lines to find out the number of instances where the values exceed $\log N_{\mathrm{O\,VII}}(\mathrm{cm}^{-2}) = 15$, the approximate sensitivity limit of X-IFU set by the systematics related to the spectral resolution (Kaastra et al. 2013). As described above, the simulation box was divided into 15 segments (5 in each orthogonal direction) of 20 Mpc length, corresponding to the X-IFU resolution. To derive predictions for SDSS we selected 6 segments for a depth of 120 Mpc, an approximation for the survey depth (130 Mpc). In practice, each of the 10 000 sight lines first crossed the whole simulation box in one random orthogonal direction and then through one segment towards a different direction. We found that in the corresponding sample ≈11% of the sight lines contain at least one absorber with $\log N_{\mathrm{O\,VII}}(\mathrm{cm}^{-2}) > 15$. We interpret this value as the probability $P_{N(\mathrm{O\,VII})}$ of encountering at least one intergalactic absorber with $\log N_{\mathrm{O\,VII}}(\mathrm{cm}^{-2}) > 15$ per random sight line through SDSS with X-IFU's resolution (see Fig. 13, left panel).

The most optimal background X-ray objects for producing the spectra to be absorbed by the intervening WHIM are presumably blazars. The current Athena Mock Observation Plan contains 39 AGN dedicated to the WHIM absorption study. The exposures are planned so that the statistical sensitivity of the X-ray signal at 20 Å is at the level of the expected systematic uncertainties (i.e. $\log N_{\mathrm{O\,VII}}(\mathrm{cm}^{-2}) \sim 15$). The AGN list is not selected based on the foreground structure and thus may be considered as a 'blind' search. The above $P_{N(\mathrm{O\,VII})} \approx 11\%$ thus applies to the sight lines towards the ∼10 AGN covered by SDSS. Thus,

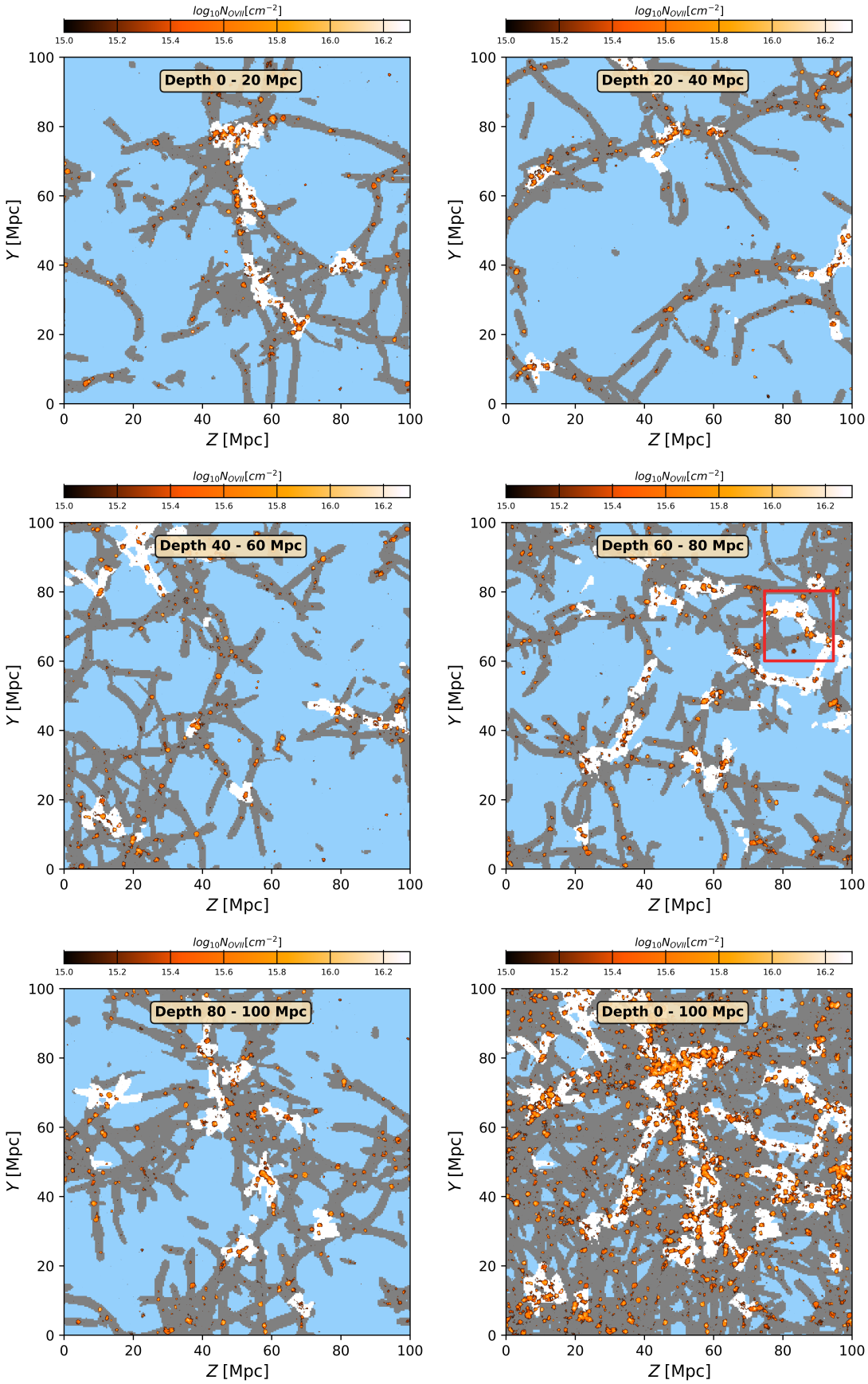

Fig. 9. O VII column densities (colour maps) above the approximate current and near-future X-ray detection limit of $\log N_{\mathrm{O\,VII}}(\mathrm{cm}^{-2}) = 15$ through slices of 20 Mpc depth along the x-axis (the *top* and *middle rows* and the *bottom-left panel*), and the combination of all slices as a projection through the whole EAGLE box (100 Mpc, *bottom-right panel*). The region covered by high LD Bisous filaments is indicated in white, while the grey area shows the region covered by the lower density filaments. The red square in the middle-right panel corresponds to the region in Fig. 7.

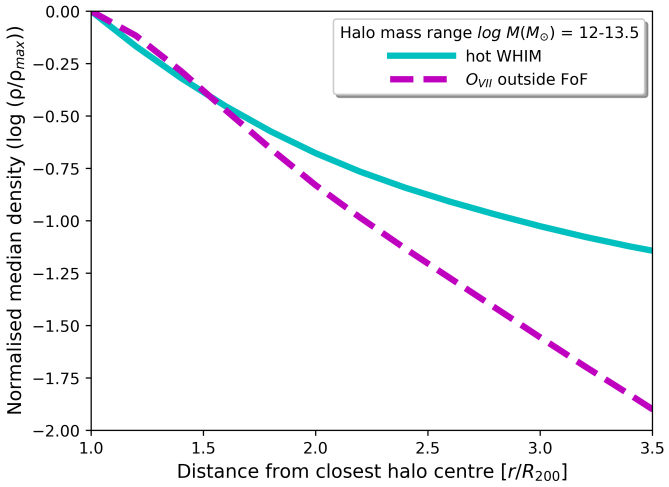

Fig. 10. Normalised density distribution of the hot WHIM (turquoise line) and O VII (dashed purple line) as a function of distance from the closest halo centre, in units of virial radius, R_{200}. As in Fig. 1, haloes were selected within the range of $\log M_{200}(M_\odot) = 12{-}13.5$.

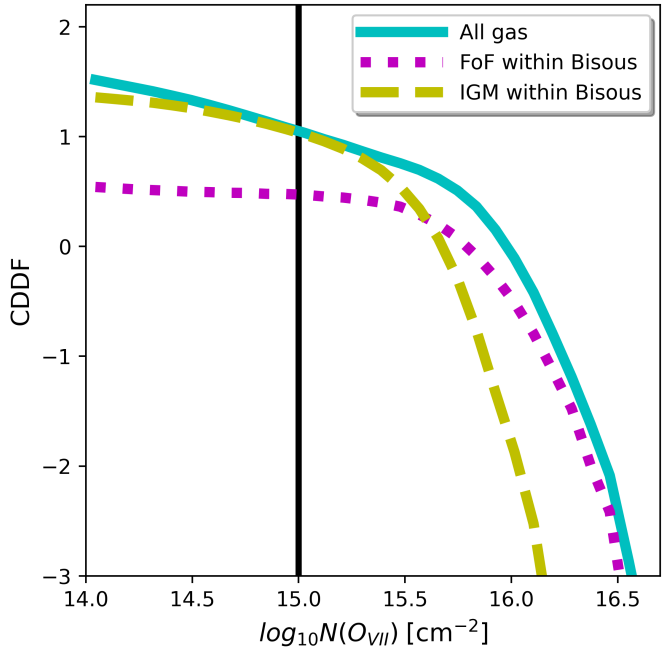

Fig. 11. CDDF of EAGLE O VII absorbers (1) in the full simulation (cyan line), (2) within FoF haloes in Bisous filaments (dotted purple line), and (3) within the IGM in Bisous filaments (dashed yellow line). The vertical black line indicates the approximate detection limit of current and near-future X-ray instruments.

we expect ∼1 intergalactic O VII detection with Athena X-IFU in the SDSS region with the currently planned AGN.

To improve the detection probability, we investigated the feasibility of targeting the optically detected filaments with Athena as an alternative to the blind search. However, as described above, the sky coverage of the full filament sample is above 90% (see the upper-left panel of Fig. 12), and thus the probability, $P_{N(\mathrm{O\,VII})}$, of detecting at least one absorber along the line of sight does not improve when focusing on filaments. We thus investigated the strategy of targeting the filaments with the highest expected WHIM density, as indicated by the highest galaxy LD (Tuominen et al. 2021). We repeated the above calculations, this time selecting only such sight lines, which cross any high LD filament (see Fig. 12). In this strategy the probability of encountering at least one absorber above Athena detection limit per sight line increases from the blind search value of ≈11% to ≈22% (see Fig. 13). While the probability doubles, the improvement remains modest due to relatively poor correlation between LD and O VII density (see Fig. 9).

5.2. 4MOST

The 4-m Multi-Object Spectroscopic Telescope (4MOST; de Jong et al. 2019) is a wide-field spectroscopic facility aimed at providing large and deep surveys of the southern sky (under development at the time of writing)[7]. One community survey in particular, the 4MOST Hemisphere Survey of the Nearby Universe (4HS), will extend the depth of a complete galaxy survey up to $z = 0.15$ (i.e. ∼600 Mpc) with a similar quality to the SDSS sample at $z = 0.05$ (described in the previous section). The higher depth of the survey will allow the construction of a robust filament sample up to $z = 0.15$. This increases the probability of randomly crossing at least one absorber of $\log N_{\mathrm{O\,VII}}(\mathrm{cm}^{-2}) > 15$ per sight line from ≈11% in SDSS to ≈45% (see Fig. 13). Targeting the high LD filaments slightly increases the probability of crossing one absorber of $\log N_{\mathrm{O\,VII}}(\mathrm{cm}^{-2}) > 15$ per sight line to a comfortable level of ≈50%.

The important improvement afforded with the 4MOST 4HS survey is the expected large (≈50%) sky coverage up to a redshift depth of $z = 0.15$. Combining this with our EAGLE-based estimate that ≈80% of the 4HS depth will be covered by high LD filaments, we expect to cover $0.5 \times 0.8 = 40\%$ of the full sky with high LD 4HS filaments. This would enable the selection of a substantial number of the brightest blazars behind these structures. We will study this issue further with the blazar flux statistics in a future work.

5.3. Limitations of simulations

As described above, the probability, $P_{N(\mathrm{O\,VII})}$, of intercepting at least one O VII absorber per sight line is rather low for absorbers above the column density limit of $\log N(\mathrm{O\,VII}) > 15$, when considering the area covered by SDSS and the depth through which the Bisous filament sample is complete (≈130 Mpc). However, this probability is highly dependant on the column density (right panel in Fig. 13). At slightly lower column densities, $\log N(\mathrm{O\,VII}) \geq 14.5$, the interception probability increases to ≈45% (≈60%) from ≈11% (≈22%) at $\log N(\mathrm{O\,VII}) > 15$ when targeting all (high LD) SDSS filaments, respectively (see Table 2 and Fig. 8 for a projection of O VII at lower column densities). The deeper surveys with 4MOST would increase the interception probability further to ≈80% (≈85%) at $\log N(\mathrm{O\,VII}) \geq 14.5$ for the full (high LD) filament samples, respectively. These levels would perhaps enable an efficient X-ray search for the absorbers.

Given that the detection probabilities are very sensitive to the simulation results around $\log N_{\mathrm{O\,VII}}(\mathrm{cm}^{-2}) \sim 15$, it is important to understand how reliable the EAGLE results are. As discussed by Mitchell & Schaye (2022), the metal transportation is very model dependant, since different simulations implement different sub-grid processes for the stellar and AGN feedback. Thus, it would be useful to compare the results of our work with those obtained using different simulations. However, different published works have different scientific aims and scopes and consequently detailed one-to-one comparison of the spread of intergalactic O VII is currently not feasible. In the following

[7] https://www.4most.eu

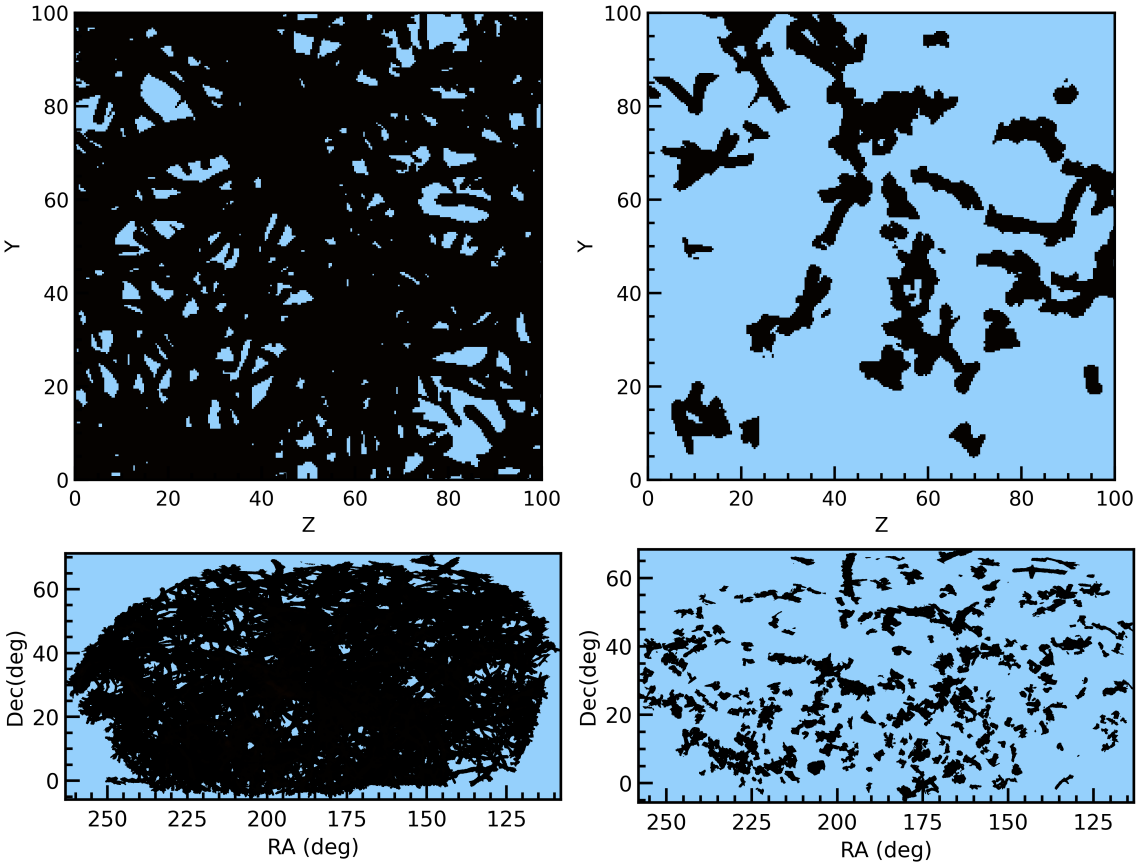

Fig. 12. Area covered by Bisous filaments in EAGLE and SDSS. *Upper-left panel*: projection of the Bisous filaments (black) along the X-direction through the whole EAGLE simulation box (100 Mpc). *Upper-right panel*: same as on the left, but selecting only filaments within high LD regions. *Lower-left panel*: Bisous filaments in the SDSS main footprint (black) projected on the plane of sky in the radial range $z = 0.02-0.05$, or ≈85−215 Mpc from Tempel et al. (2014). *Lower-right panel*: same as on the left, but selecting only filaments within high LD regions.

we place our results in the context of other simulations to the extent allowed by the current literature.

Mitchell & Schaye (2022) studied the transportation of metals within and beyond haloes in EAGLE. They found that the mass of metals ejected outside R_{200} peaks at halo masses $M_{200}(z = 0) \sim 10^{12-13}\,M_\odot$. The ejected metal mass is substantial; is it similar to that remaining inside R_{200} (in stars, ISM and CGM). At the same time, however, they commented that the model used for mixing the metals with pristine gas is not yet at an advanced level. This might affect the amount of the metals ejected into intergalactic space in the EAGLE simulations.

In a similar vein, Chadayammuri et al. (2022) found that the EAGLE simulation overpredicts the X-ray emission of the stacked eROSITA data of a sample of over 2000 galaxies in the central 100 kpc region for galaxies of stellar mass of $M_* \sim 10^{11}\,M_\odot$. They speculated that the AGN feedback model in EAGLE is not efficient enough in blowing the gas out. Chadayammuri et al. (2022) point out that $M_* \sim 10^{11}\,M_\odot$ galaxies in Illustris-TNG simulation better fit the eROSITA data, possibly because it is calibrated to better reproduce the baryon content within groups and clusters. Consistently with the above, the EAGLE gas mass fraction in $\log M(M_\odot) = 13-14$ haloes within R_{500} is higher than that in the Illustris-TNG and Magneticum simulations (Fig. 2, left panel Lim et al. 2021), suggesting a weaker EAGLE feedback for haloes within this mass range.

In SIMBA simulations (Davé et al. 2019), the majority of the O VII ions are located outside the virial radii of the haloes. The density peaks at $\sim 2-3 \times R_{200}$ distance from the nearest halo, predominantly within the filaments of the Cosmic Web (Bradley et al. 2022). This behaviour is somewhat different from what we obtain in the EAGLE simulations, where the O VII density decreases beyond the virial radius. While the essential difference between the SIMBA and EAGLE simulations is the implementation of bipolar kinetic outflows from the AGN in the former, the runs without jets give almost identical results. Thus, it is not currently clear what is causing the difference.

However, the comparison of the results from SIMBA and EAGLE simulations is consistent with the above suggestion that EAGLE underestimates the ejection of metals from haloes into the IGM. In this case the detection probabilities of the intergalactic O VII presented in our work would be too small, as more absorbing systems would have densities above the limiting column density of $\log N(\mathrm{O\,VII}) > 15$ in the intergalactic space. We will investigate this issue in future work by analysing cosmological simulations with significantly different recipes for the metal enrichment.

6. Conclusions

In this work we have analysed the distribution of the intergalactic oxygen atoms and O VII ions within the filaments of the Cosmic Web in the EAGLE simulation. Since oxygen is formed in and expelled from galaxies, we also studied the surroundings of haloes. We characterised the spatial distributions of oxygen and O VII and studied their mass and volume fill-

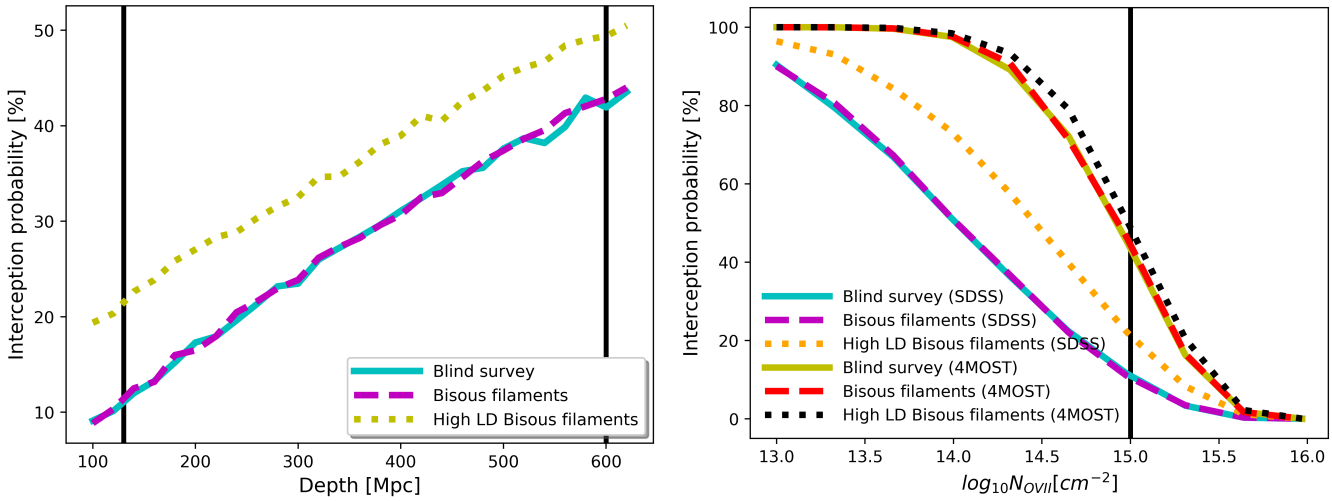

Fig. 13. EAGLE-based probability of intercepting an intergalactic O VII absorber (see Sect. 5 for our definition of such an absorber). *Left panel*: probability for an absorber with column density $\log N_{\rm O\,VII}({\rm cm}^{-2}) > 15$ indicated as a function of the probed path length (1) for a blind search (solid turquoise line), (2) when targeting Bisous filaments (dashed purple line), and (3) when targeting high LD Bisous filaments (dotted orange line). The vertical black lines indicate the depths of the SDSS survey (left) and 4MOST 4HS survey (right). *Right panel*: interception probability in different filament targeting scenarios along a 130 (600) Mpc path corresponding to the SDSS (4MOST) samples discussed in the text: no targeting (solid turquoise and yellow lines), targeting Bisous filaments (dashed purple and red lines), and targeting high LD Bisous filaments (dotted orange and black lines). The vertical solid black line indicates the approximate detection level of current and near-future X-ray absorption instruments.

ing fractions in the filaments. We used this information to estimate the fraction of hot WHIM that can potentially be traced by O VII, as well as the feasibility of detecting intergalactic O VII absorbers with Athena X-IFU. Here we summarise our main conclusions:

1. The projected areas covered by filaments detected with the Bisous formalism (Tempel et al. 2014) in the observational SDSS survey and in the EAGLE simulation mask over 90% of the total area. In addition, both observations and the simulation agree to within 1%, indicating that the basic geometric properties of the filaments, that is, number densities and sizes, are properly reproduced in the EAGLE simulation.
2. Of all the intergalactic oxygen within Bisous filaments, ≈72% lies above the hot WHIM temperature limit of $\log T({\rm K}) > 5.5$. Consequently, ≈33% of the intergalactic filamentary oxygen has been ionised to O VII.
3. According to the EAGLE simulations, the density profiles of the intergalactic O VII decline rapidly beyond the virial radius of haloes. The median radial extent of O VII above the approximate Athena X-IFU detection limit is ≈700 kpc when an optimal observation scenario is considered.
4. Since galaxies are relatively far apart from one another, filaments are not fully filled with intergalactic O VII at densities above the approximate Athena X-IFU detection limit. Indeed, the volume filling fraction is ∼1% of the total filament volume. This implies that most of the O VII detectable with Athena X-IFU is located within small envelopes around haloes.
5. The highly inhomogeneous distribution of the detectable O VII complicates the usage of the measurements of the intergalactic O VII absorbers for tracing the missing baryons and estimating their contribution to the cosmic baryon budget. Nonetheless, a significant fraction of the hot WHIM (≈27%) may be traced with intergalactic O VII.
6. The probability of encountering an intergalactic O VII absorber with $\log N_{\rm O\,VII}({\rm cm}^{-2}) > 15$ in the filament sample obtained by Tempel et al. (2014) from the optical spectroscopic SDSS galaxy survey is 10−20% per sight line. The expected extension of the path lengths through filaments afforded by the advent of 4MOST surveys will improve the probability to a comfortable level of ∼50%.
7. The probability of intercepting a detectable O VII absorber is very sensitive to the column density. Thus, if in reality feedback processes are more effective at expelling metals into the IGM than those implemented in EAGLE, the estimates for the interception probability will be larger. Similarly, slight improvements in the O VII absorption sensitivity with instruments beyond the X-IFU limit would significantly boost the probability of intercepting an absorbing system.

Based on EAGLE, the amount of missing baryons that is expected to be traceable with next-generation X-ray instruments is limited to the immediate vicinity of haloes. Since a significant fraction of baryons lie in the diffuse intergalactic regime, probing only the high-density regions around haloes would fall short of accounting for the whole of the missing baryons. Nonetheless, a significant fraction of the missing baryon mass (≈7−27%) resides in the outskirts of haloes beyond the virial radius, R_{200}. Thus, Athena X-IFU will provide invaluable observations for reducing the amount of missing baryons.

Acknowledgements. We would like to thank Joop Schaye for his invaluable comments. We also thank the referee for their helpful and educated suggestions. We acknowledge the support by the Estonian Research Council grants PRG1006, and by the European Regional Development Fund (TK133). We acknowledge the Virgo Consortium for making their simulation data available. The eagle simulations were performed using the DiRAC-2 facility at Durham, managed by the ICC, and the PRACE facility Curie based in France at TGCC, CEA, Bruyères-le-Châtel.

References

Ahn, C. P., Alexandroff, R., Allende Prieto, C., et al. 2014, ApJS, 211, 17
Aragón-Calvo, M. A., Jones, B. J. T., van de Weygaert, R., & van der Hulst, J. M. 2007, A&A, 474, 315
Barret, D., Lam Trong, T., den Herder, J. W., et al. 2018, SPIE Conf. Ser., 10699, 106991G
Bertone, S., Schaye, J., Dalla Vecchia, C., et al. 2010, MNRAS, 407, 544

Bradley, L., Davé, R., Cui, W., Smith, B., & Sorini, D. 2022, arXiv e-prints [arXiv:2203.15055]
Branchini, E., Ursino, E., Corsi, A., et al. 2009, ApJ, 697, 328
Bregman, J. N. 2007, ARA&A, 45, 221
Bykov, A. M., Paerels, F. B. S., & Petrosian, V. 2008, Space Sci. Rev., 134, 141
Cautun, M., van de Weygaert, R., & Jones, B. J. T. 2013, MNRAS, 429, 1286
Cautun, M., van de Weygaert, R., Jones, B. J. T., & Frenk, C. S. 2014, MNRAS, 441, 2923
Cen, R., & Ostriker, J. P. 1999, ApJ, 514, 1
Cen, R., & Ostriker, J. P. 2006, ApJ, 650, 560
Chadayammuri, U., Bogdán, Á., Oppenheimer, B. D., et al. 2022, ApJ, 936, L15
Crain, R. A., Schaye, J., Bower, R. G., et al. 2015, MNRAS, 450, 1937
Cui, W., Borgani, S., Dolag, K., Murante, G., & Tornatore, L. 2012, MNRAS, 423, 2279
Cui, W., Knebe, A., Yepes, G., et al. 2018, MNRAS, 473, 68
Cui, W., Chen, L., Gao, B., et al. 2020, J. Low Temp Phys., 199, 502
Damle, M., Sparre, M., Richter, P., et al. 2022, MNRAS, 512, 3717
Davé, R., Cen, R., Ostriker, J. P., et al. 2001, ApJ, 552, 473
Davé, R., Anglés-Alcázar, D., Narayanan, D., et al. 2019, MNRAS, 486, 2827
de Graaff, A., Cai, Y.-C., Heymans, C., & Peacock, J. A. 2019, A&A, 624, A48
de Jong, R. S., Agertz, O., Berbel, A. A., et al. 2019, The Messenger, 175, 3
Dolag, K., Meneghetti, M., Moscardini, L., Rasia, E., & Bonaldi, A. 2006, MNRAS, 370, 656
Dolag, K., Borgani, S., Murante, G., & Springel, V. 2009, MNRAS, 399, 497
Ferland, G. J., Korista, K. T., Verner, D. A., et al. 1998, PASP, 110, 761
Galárraga-Espinosa, D., Aghanim, N., Langer, M., Gouin, C., & Malavasi, N. 2020, A&A, 641, A173
Galárraga-Espinosa, D., Aghanim, N., Langer, M., & Tanimura, H. 2021, A&A, 649, A117
Ganeshaiah Veena, P., Cautun, M., Tempel, E., van de Weygaert, R., & Frenk, C. S. 2019, MNRAS, 487, 1607
Gaskin, J. A., Swartz, D. A., Vikhlinin, A., et al. 2019, J. Astron. Telesc. Instrum. Syst., 5, 021001
Haardt, F., & Madau, P. 2001, in Clusters of Galaxies and the High Redshift Universe Observed in X-rays, eds. D. M. Neumann, & J. T. V. Tran, 64
Haider, M., Steinhauser, D., Vogelsberger, M., et al. 2016, MNRAS, 457, 3024
Holt, P., Tuominen, T., Nevalainen, J., et al. 2022, MNRAS, 513, 3387
Kaastra, J. S. 2017, Astron. Nachr., 338, 146
Kaastra, J., Finoguenov, A., Nicastro, F., et al. 2013, arXiv e-prints [arXiv:1306.2324]
Kelly, A. J., Jenkins, A., Deason, A., et al. 2022, MNRAS, 514, 3113
Kuutma, T., Poudel, A., Einasto, M., et al. 2020, A&A, 639, A71
Liivamägi, L. J., Tempel, E., & Saar, E. 2012, A&A, 539, A80
Lim, S. H., Barnes, D., Vogelsberger, M., et al. 2021, MNRAS, 504, 5131
Macquart, J. P., Prochaska, J. X., McQuinn, M., et al. 2020, Nature, 581, 391
Martizzi, D., Vogelsberger, M., Artale, M. C., et al. 2019, MNRAS, 486, 3766
Mazzotta, P., Mazzitelli, G., Colafrancesco, S., & Vittorio, N. 1998, A&AS, 133, 403
McAlpine, S., Helly, J. C., Schaller, M., et al. 2016, Astron. Comput., 15, 72
Mitchell, P. D., & Schaye, J. 2022, MNRAS, 511, 2600
Muru, M. M., & Tempel, E. 2021, A&A, 649, A108
Nandra, K., Barret, D., Barcons, X., et al. 2013, arXiv e-prints [arXiv:1306.2307]
Nelson, D., Kauffmann, G., Pillepich, A., et al. 2018, MNRAS, 477, 450
Nevalainen, J., Tempel, E., Liivamägi, L. J., et al. 2015, A&A, 583, A142
Nevalainen, J., Wakker, B., Kaastra, J., et al. 2017, A&A, 605, A47
Nevalainen, J., Tempel, E., Ahoranta, J., et al. 2019, A&A, 621, A88
Nicastro, F., Fang, T., & Mathur, S. 2022, arXiv e-prints [arXiv:2203.15666]
Planck Collaboration I. 2014, A&A, 571, A1
Planck Collaboration XXII. 2016, A&A, 594, A22
Rasmussen, A. P., Kahn, S. M., Paerels, F., et al. 2007, ApJ, 656, 129
Ryu, D., Kang, H., Hallman, E., & Jones, T. W. 2003, ApJ, 593, 599
Schaller, M., Dalla Vecchia, C., Schaye, J., et al. 2015, MNRAS, 454, 2277
Schaye, J., Crain, R. A., Bower, R. G., et al. 2015, MNRAS, 446, 521
Shull, J. M., Smith, B. D., & Danforth, C. W. 2012, ApJ, 759, 23
Smith, R. K., Abraham, M., Baird, G., et al. 2019, SPIE Conf. Ser., 11118, 111180W
Snowden, S. L., Egger, R., Freyberg, M. J., et al. 1997, ApJ, 485, 125
Sousbie, T. 2011, MNRAS, 414, 350
Springel, V. 2005, MNRAS, 364, 1105
Springel, V., White, S. D. M., Tormen, G., & Kauffmann, G. 2001, MNRAS, 328, 726
Stoica, R. S., Martínez, V. J., & Saar, E. 2007, J. R. Stat. Soc.: Ser. C (Appl. Stat.), 56, 459
Stoica, R. S., Martínez, V. J., & Saar, E. 2010, A&A, 510, A38
Strawn, C., Fàbrega, S. R., & Primack, J. 2023, MNRAS, 519, 1
Tanimura, H., Hinshaw, G., McCarthy, I. G., et al. 2019, MNRAS, 483, 223
Tanimura, H., Aghanim, N., Bonjean, V., Malavasi, N., & Douspis, M. 2020a, A&A, 637, A41
Tanimura, H., Aghanim, N., Kolodzig, A., Douspis, M., & Malavasi, N. 2020b, A&A, 643, L2
Tempel, E., Einasto, J., Einasto, M., Saar, E., & Tago, E. 2009, A&A, 495, 37
Tempel, E., Stoica, R. S., Martínez, V. J., et al. 2014, MNRAS, 438, 3465
Tempel, E., Stoica, R. S., Kipper, R., & Saar, E. 2016, Astron. Comput., 16, 17
Tepper-García, T., Richter, P., Schaye, J., et al. 2012, MNRAS, 425, 1640
Tuominen, T., Nevalainen, J., Tempel, E., et al. 2021, A&A, 646, A156
Wendland, H. 1995, Adv. Comput. Math., 4, 389
Wiersma, R. P. C., Schaye, J., Theuns, T., Dalla Vecchia, C., & Tornatore, L. 2009a, MNRAS, 399, 574
Wiersma, R. P. C., Schaye, J., & Smith, B. D. 2009b, MNRAS, 393, 99
Wijers, N. A., & Schaye, J. 2022, MNRAS, 514, 5214
Wijers, N. A., Schaye, J., Oppenheimer, B. D., Crain, R. A., & Nicastro, F. 2019, MNRAS, 488, 2947
Wijers, N. A., Schaye, J., & Oppenheimer, B. D. 2020, MNRAS, 498, 574